

5 **Estimation of the Escape of Photoelectrons from Mars in
2004
Liberated by the Ionization of Carbon Dioxide
and Atomic Oxygen**

10 R. A. Frahm,^{a*} J. R. Sharber,^a J. D. Winningham,^a R. Link,^b

 M. W. Liemohn,^c J. U. Kozyra,^c A. J. Coates,^d D. R. Linder,^d

15 S. Barabash,^e R. Lundin,^e A. Fedorov^f

^a Southwest Research Institute, PO Drawer 28510, 6220 Culebra Road, San Antonio, TX
 78228-0510, USA

20 Corresponding Author E-mail Adders: rfrahm@swri.edu

^b Radiation Safety Institute of Canada, 1120 Finch Ave. W., Suite 607, Toronto ON, M3J-3H7,
 Canada

25 ^c Space Physics Research Laboratory, University of Michigan, Ann Arbor, MI 48109-2143,
 USA

^d Mullard Space Science Laboratory, University College London, Surrey RH5 6NT, UK

30 ^e Swedish Institute of Space Physics, Box 812, SE-981 28 Kiruna, Sweden

^f Centre d'Etude Spatiale des Rayonnements, BP-4346, F-31028 Toulouse, France

35 Pages: 57

40 Tables: 2

 Figures: 14

Proposed Running Head: 2004 Mars photoelectron escape

45

Editorial correspondence to:

50 Dr. Rudy A. Frahm
Department of Space Sciences
Southwest Research Institutes
6220 Culebra Road
P.O. Drawer 28510
55 San Antonio, TX 78238
Phone: +1-210-522-3855
Fax: +1-210-647-4325
E-mail address: rfrahm@swri.edu

Abstract

60

Photoelectron peaks in the atmosphere of Mars caused by the ionization of carbon dioxide and atomic oxygen by solar 30.4 nm photons have been observed by the Electron Spectrometer (ELS), a component of the Mars Express (MEx) Analyzer of Space Plasmas and Energetic Atoms (ASPERA-3) experiment. Ionization mostly occurs at the Mars exobase with the

65

majority of the photoionized electron flux trapped in the remanent and induced magnetic field, with a portion of that flux escaping the planet down its tail. Since Mars is overall charge neutral, the number of electrons must be identical to the number of ion charges which escape the planet.

An estimate of the fraction of the total number of escaping electrons is obtained for the year 2004, specifically those produced by the ionization of carbon dioxide and atomic oxygen by

70

solar 30.4 nm photons. In achieving this process, an illustrative example pass is used to show how the electron spectrum is adjusted for the potential on the spacecraft; then the region of the electron spectrum which shows photoelectron peaks is integrated over energy, yielding a flux of 5.74×10^6 electrons/(cm² s sr). This technique is then applied to a subset of 22 sample averaged spectra from the 2004 data (5 January 2004 through 25 January 2005), yielding an average result

75

of 4.15×10^6 electrons/(cm² s sr) for the 22 cases. The observation cone of 33.75° is used to integrate over solid angle (assuming the flux is constant), giving 4.39×10^6 electrons/(cm² s).

This average value was taken as representative of the full data interval. Frequency of occurrence statistics showing about a 6.2% occurrence rate for the 2004 data is applied to give an average escape flux from Mars of 2.72×10^5 electrons/(cm² s) during 2004. By estimating the outflow

80

area as 1.16×10^{18} cm² at $X = -1.5 R_{\text{Mars}}$ the electron escape rate of 3.14×10^{23} electrons/s is obtained. Thus about 9.92×10^{30} electrons or 16.5 Mmole of electrons escaped Mars during 2004 due to the ionization of carbon dioxide and atomic oxygen by the He 30.4 nm line. Due to

the caveats of the analysis, these derived escape rates should be considered lower limits on the total electron escape rate from Mars.

85

Key Words: Atmospheres, evolution; Ionospheres; Mars

1. Introduction

90

When the solar wind encounters an obstacle its reaction is dependent on the properties of that obstacle. Some obstacles possess no atmosphere/ionosphere or magnetic field like the Earth's moon. Others possess an atmosphere/ionosphere, but have no internal magnetic field, like Venus. Mars is an example of an obstacle which possess an atmosphere/ionosphere and has
95 no internal magnetic field, but does possess remanent crustal magnetic fields (Acuña et al., 1998). The Earth is an example of an obstacle which has both an atmosphere/ionosphere and an internal magnetic field. An obstacle such as Mars stands off the solar wind through a complicated mechanism of deflecting the solar wind around the planet. This occurs when a bow shock is formed in front of the planet to deflect the solar wind plasma around the planet, while
100 currents flow in the upper atmosphere/ionosphere to stand off and divert the solar wind's magnetic field. The current flow causes an induced magnetic cavity to be formed around the obstacle.

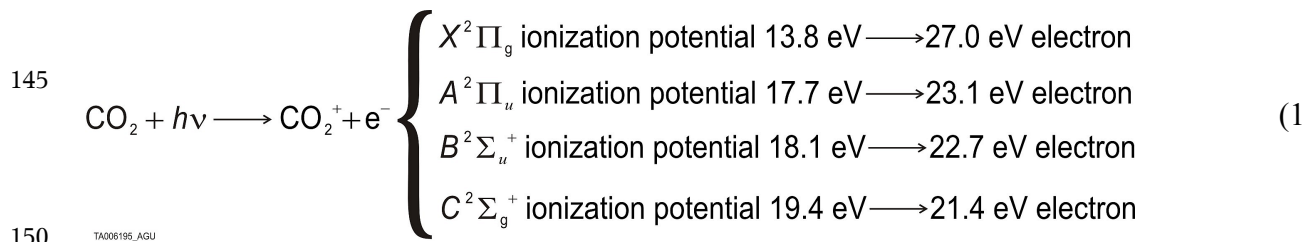
The location of the magnetic cavity boundary is called the Induced Magnetic Boundary (IMB) and was described by Lundin et al. (2004). At the same location, the solar wind magnetic
105 field piles-up as it slips around the planet in what is also referred to as the Magnetic Pile-up Boundary (MPB) (Acuña et al., 1998). Multiple boundary names have been given to various locations at Mars depending on how they are measured and a summary of them can be found in Duru et al. (this issue).

As part of the solar wind-Mars interaction, some of the atmosphere of Mars is stripped
110 away from the planet. This escaping plasma has been computed using ion measurements from various spacecraft missions. Using ion measurements from the Phobos-2 mission obtained near

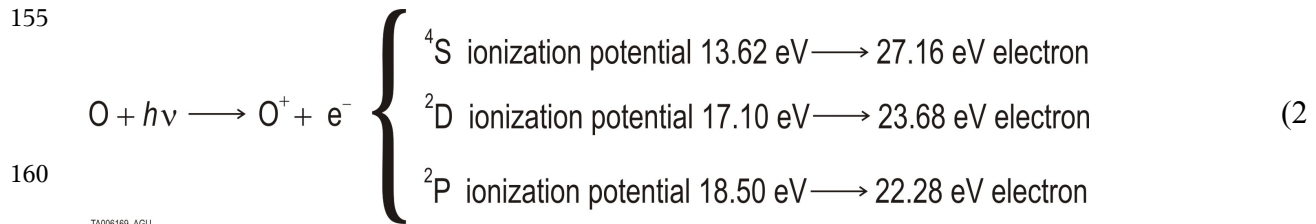
solar maximum, Lundin et al. (1989, 1990) estimated an oxygen escape rate of about $3 \times 10^{25} \text{ s}^{-1}$ while Verigin et al. (1991) determined the loss of ions from the plasma sheet to be about $5 \times 10^{24} \text{ s}^{-1}$. From the Mars Express (MEx) spacecraft at solar minimum, Dubinin et al. (2006) found a total escape rate of between $6 \times 10^{23} \text{ s}^{-1}$ and $6 \times 10^{24} \text{ s}^{-1}$, while Carlsson et al. (2006) estimated the CO_2^+ loss rate to be $4.0 \times 10^{24} \text{ s}^{-1}$ by normalizing MEx measurements to that obtained from the Phobos-2 mission. Barabash et al. (2007), using MEx measurements refined these numbers to determine an O^+ loss rate of $1.6 \times 10^{23} \text{ s}^{-1}$, an O_2^+ loss rate of $1.5 \times 10^{23} \text{ s}^{-1}$, and a CO_2^+ loss rate of $8 \times 10^{22} \text{ s}^{-1}$. Mars atmospheric erosion rates determined so far have been preformed using ion measurements. In May of 2007, the performance of the MEx ion instrument was modified to increase the energy resolution at low ion energies which increased its sensitivity to cold/low-energy ions ($\leq 10 \text{ eV}$). Due primarily to the inclusion of this cold ion population, analysis of ion measurements made after this modification yielded higher escape rates, in particular $2.4 \times 10^{24} \text{ ions/s}$ for O^+ and $3.3 \times 10^{24} \text{ ions/s}$ for the total heavy ion rate (Lundin et al., 2008a,b). Mars atmospheric erosion rates using electron measurements are difficult because the bulk flow velocities are low and measurements are often influenced by the spacecraft, which combine to make loss rate determinations difficult. In addition, the flow rates are determined from differences of hemispherically measured flux rates, often resulting in taking differences between large values.

130 Since December 25, 2003, the MEx spacecraft has been orbiting Mars. MEx measurements of the Martian particle environment have been performed by the Analyzer of Space Plasmas and Energetic Atoms (ASPERA-3) Experiment (Barabash et al., 2004), which measures electrons with the Electron Spectrometer (ELS), ions with the Ion Mass Analyzer (IMA), and neutral particles with the Neutral Particle Detector (NPD) and Neutral Particle

135 Imager (NPI). Since arriving at Mars, ELS has measured peaks in the photoelectron spectrum
 (Lundin et al., 2004). These photoelectron peaks are attributed to both carbon dioxide and
 atomic oxygen, and are theoretically located in energy between 21 eV and 24 eV, and 27 eV
 (Mantas and Hanson, 1979; Fox and Dalgarno, 1979). The relevant photoelectron peaks in the
 energy spectrum are mainly due to ionization by solar 30.4 nm photons. More specifically for
 140 carbon dioxide the following ionizations are described by Padial et al. (1981) and the ejected
 photoelectron is computed for a solar 30.4 nm photon:



For atomic oxygen, the ionization states are described by Mantas and Hanson (1979) and the
 ejected photoelectron is also computed for a solar 30.4 nm photon:



The ELS observations of photoelectron peaks in the energy spectrum are mainly due to
 165 ionization of carbon dioxide near the Martian exobase with subsequent transport to higher
 altitudes (Mantas and Hanson, 1979). Near the Martian exobase, the concentration of carbon
 dioxide is about 50 times greater than atomic oxygen. The energy resolution of ELS (about 8%)
 is too large to distinguish between the energy spectrum of electrons photoionized from carbon
 dioxide and those from atomic oxygen. At altitudes above about 210 km, atomic oxygen

170 becomes the dominant species over carbon dioxide (down by about a factor of 1000 from its
peak production rate) and the atomic oxygen to carbon dioxide ratio continues to increase even
though the amount of atomic oxygen exponentially decreases (Krasnopolsky and Gladstone,
1996). At spacecraft altitudes, locally produced electrons from ionization of the atomic oxygen
(above 250 km) occur more frequently than by locally produced electrons from ionization of
175 carbon dioxide. ELS can not distinguish between photoelectrons produced locally and those
transported to the sensor.

After ionization of the carbon dioxide or atomic oxygen, the charged components are
subject to the local magnetic field and are transported accordingly (Mantas and Hanson, 1979).
More recently, Uluşen and Linscott (2008) have invoked a similar transport mechanism to
180 explain the observation of enhanced electron flux at the west edge of crustal field regions. The
ASPERA-3 ELS has observed photoelectron peaks in the Martian induced magnetosphere while
orbiting the planet at various altitudes (Frahm et al, 2006a,b; Liemohn et al., 2006a). Low-
energy planetary ions in the Martian ionosphere have been detected by the IMA that are
components of carbon dioxide. Ions in the Martian ionosphere are observed to be directional;
185 however, their low-energies are near the IMA energy threshold. Detection may be a result of ion
flow caused by the ram pressure of the spacecraft motion combined with spacecraft potential
(i.e., not a real flow).

In this presentation we show an example spacecraft pass which exhibits peaks in the
photoelectron spectrum in the Martian ionosphere along with the low-energy ions measured at
190 the same location. We also show electron spectra which exhibit photoelectron peaks in the
Martian tail on the same orbit. The photoelectron spectra exhibit similar intensities compared to
those which have previously been measured (see examples in Frahm et al., 2006a,b), and there

is nothing special about the photoelectron spectrum used; however, escape rate estimates derived in this paper are dependent on the averaged electron spectrum used in the computation. The purpose of this study is to use this averaged spectrum and our previous results (Frahm et al., 2006b; Liemohn et al., 2006b) that photoelectrons from the Martian atmosphere are being transported down the Martian tail in order to estimate the atmospheric electron loss in 2004 due to ionizations of carbon dioxide and atomic oxygen by HeII 30.4 nm photons.

The outflow of electrons included within the photoelectron peaks at Mars should be taken as an estimate. Rigorous electron outflow measurements require a three-dimensional electron instrument which has a low enough threshold, a large enough energy range, high enough fidelity, and fine enough energy, angle, and temporal resolution in order to distinguish real flux differences. In any planetary investigation, there needs to be an independent vector magnetometer to orient the electron measurements and a separate independent measure of the spacecraft potential. To date, no spacecraft flown to Mars has met these requirements. MEx does not contain a magnetometer experiment nor an independent way to determine spacecraft potential. The ASPERA-3 ELS provides only a two-dimensional measurement of the electron distribution and the orientation of its measurement plane is independent of the magnetic field. The determination of spacecraft potential is highly dependent on the location and spectral appearance of electron features from the dayside Mars ionosphere. The estimate obtained is determined by a state-of-the-art electron instrument which falls short of the intense rigor required, but in this paper it will be used to estimate the electron outflow rate at Mars in 2004.

Since Mars is observed to be charge neutral, the outflow of electrons must be about the same as that of ions. However, this electron escape rate should be determined for all electrons just as the ion escape rate must be determined for all ions. In this paper, we will only determine

the electron loss rate from the subset of electrons liberated during the photoionization processes described by equations 1 and 2. Since Carlsson et al. (2006) have stated that the most abundant ion species measured by IMA are O^+ , O_2^+ , and CO_2^+ , we should keep in mind the total ion escape rates for these species and compare them to that obtained from electrons. If the escape rate of photoelectrons generated by the processes described by equations 1 and 2 is significantly larger than the ion escape rate, then the ions liberated in the photoionization process must undergo further atmospheric/ionospheric interactions and the loss rates of other ion species must be significant. If the electron escape is significantly less than the ion escape, then the photoionization process does not play a significant role in the plasma escape process and other mechanisms are significant.

2. Instrument

The ASPERA-3 *in situ* measurements on the MEx spacecraft are performed by ELS and IMA. The ELS is a spherical top hat electrostatic analyzer with a symmetric collimator baffle and light trap system. Incoming electrons passing through the baffle system are deflected onto a microchannel plate and anode system containing sixteen 22.5° sectors in the instrument measurement plane (perpendicular to the symmetry axis). Differential measurements are made within the energy range 1 eV to 20 keV. Table 1 shows the energy conversion factors and energy resolutions for each angular sector based on laboratory calibrations.

[Table 1]

Of the possible 8192 voltage values generated by the ELS power supplies, 128 values are normally selected to form the ELS energy sweep. These 128 voltage values can be the same or

different, and form a 4 s sweep sequence. Currently there are three types of sweep sequences in
240 use by ELS. In the first, all 128 values have the same voltage, producing a single energy step in
the energy sweep. In the second, a sequence of 32 voltage steps are chosen to form the sweep
and this sequence is repeated four times during the 4 s sequence (31 sequentially decreasing
voltage values with one flyback step), effectively generating a 1 s energy sweep of 31 energy
values. The third, and normal energy sweep, is a sequence of 128 voltage steps, generating a
245 127 step energy sweep with one flyback step . This mode provides a spectrum of continuous
energy samples every 4 s. Data used in this paper are collected from both 1 and 4 s energy
sweeps.

The IMA measures ions up to 40 amu within the energy range 10 eV to 60 keV. The
instrument is cylindrically symmetric with the measurements made over 16 azimuthal sectors of
250 22.5° each. Using electrostatic deflection, ions are selected in sixteen 5.5° polar angle sectors
within $\pm 45^\circ$ of the instrument measurement plane (the plane perpendicular to the symmetry
axis). In the normal mode these ions are analyzed in 96 energy steps as they pass through a top
hat electrostatic analyzer after which they are separated radially by mass into 32 concentric rings
by means of permanent sector magnets. The maximum spectral resolution results from 32
255 masses x 16 azimuthal sectors x 96 energy steps x 16 polar angles. A time of 192 s is required
for the complete measurement sequence. Further details of ELS and IMA may be found in
Barabash et al. (2004; 2006).

Since launch some changes in IMA operational capability (not discussed in the
instrument papers) have been implemented. One of these reduces the time required in order to
260 complete the spectral measurement sequence by reducing the number of polar angles and/or
energy steps. Another change has been made to improve the energy resolution at low energies.

Initially, IMA was tuned to concentrate energy resolution at the higher energies of the measurement range; however, as of 30 April 2007, the IMA energy resolution was re-tuned to emphasize lower energies. In this mode, the polar angle deflection system is disabled when IMA
265 is analyzing ions with energies below 50 eV, in which case ions enter from about $\pm 2.5^\circ$ of IMA's measurement plane.

3. Data

270 The ELS instrument can resolve two peaks in the electron spectrum which are due to electrons generated during the carbon dioxide/atomic oxygen photoionization process. These peaks are clear in the oversampling mode, but the dual peak structure is not as obvious at times due to the phasing of the energy sampling with respect to the plasma. We illustrate this by presenting a simulation of the ELS instrument in which the sampled electron plasma distribution
275 is that described by Mantas and Hanson (1979). In Figure 1, the sampled electron plasma is drawn as a continuous solid green line which was linearly interpolated between each datum of Mantas and Hanson's values. The ELS simulated response to this plasma uses the energy resolution of an ELS sector along with the assumption that the electron plasma fills the entire angular measurement range of that sector. As a part of the simulation the resulting measured
280 values are converted to integer count values in a 16-bit register, compressed to an 8-bit value simulating a lossy telemetry compression, decompressed to a 16-bit integer simulating decompression on the ground, and then converted into differential number flux values using simulated instrument characteristics. These values are shown as blue dots at the center energy for each measurement in the energy sweep. Poisson statistics are then applied to the instrument

285 counts to estimate the error range, which is then drawn as blue error bars on each datum. The location of the two count sensitivity is shown as a dotted red line for reference. Values below 70 eV are shown both in log energy space (a) and in linear energy space (b).

[Figure 1]

290 In Figure 1, data are simulated for the normal energy sampling mode of 128 energy steps in a 4 sec energy sweep. This figure represents a “best case” example of sampling a spectrum in which the energy channel is aligned with the 27 eV energy peak in the electron plasma and the low energy peak between 21 eV and 24 eV contains more than one simulated measurement sample. Two distinct energy peaks can be observed by eye in this 21-27 eV region of the spectrum.

295 When the spacecraft charges, the peaks will appear to be shifted in energy, and this can cause the electron plasma to be sampled at energy locations which are not optimal for peak resolution. This is investigated using the same plasma simulation where the center of the ELS energy channels are shifted by half an energy channel width. The result is shown in Figure 2 using the same format as Figure 1. In this case only the lower energy (21-24 eV) is discerned as
300 a sharp peak. The higher energy (27 eV) peak appears as a ledge and is not easily discerned as a peak.

[Figure 2]

In most cases, the observed energy spectrum will lie between the two extreme cases shown by Figures 1 and 2. At most times there are two distinct energy peaks observed. The
305 exact pattern observed is a function of the spacecraft charge as it will control where, in energy space, the peaks from the carbon dioxide/atomic oxygen process will fall. However, it is important to note that the energy structure of the measured peaks exhibits an energy width

profile which either shows a twin peak structure (one peak at ground state ionization separated by a larger peak for the remaining ionizations) or a flat structure at the location of the ground
310 state ionization separated by a larger peak for the remaining ionization when sampled by ELS
under normal energy resolution.

3.1. Selected Orbit

315 Photoelectron peaks are observed on almost every transit of the spacecraft through the
ionosphere. Figure 3 shows an orbit of the MEx spacecraft on 19 June 2007 in cylindrical Mars-
centered Solar Orbital (MSO) coordinates (the X-axis points toward the Sun, The Z-axis is
perpendicular to the planet's velocity vector in the northern ecliptic plane, and the Y-axis
completes the right handed system). On this figure, the Sun is at the left. The average shapes of
320 the bow shock and magnetopause are determined by Vignes et al. (2000) are drawn in blue. The
trajectory of MEx is marked in red with tick marks every 10 minutes and time labels every hour.
The pericenter of MEx is marked with a green circle and orbit numbers are computed at
apocenter crossings, which is marked with two green circles on the MEx trajectory. Vertical
black lines break the MEx trajectory, with orbit 4439 being shown prior to 1906 UT and
325 orbit 4440 being shown after 1906 UT (the orbit number counter definition occurs at the location
of the apocenter markings). The general locations where photoelectron peaks are observed in the
electron spectrum are shown as shaded regions along the spacecraft orbit.

[Figure 3]

In this pass, the ELS data place the location of the magnetopause at a lower radial
330 distance to the X-axis than the average position predicted by Vignes et al. (2000). The location

of the magnetopause derived from the ELS data is noted on Figure 3 in green. This pass was chosen because electron spectra showing carbon dioxide and atomic oxygen photoionization peaks are observed both in the ionosphere and far down the tail of Mars, and ELS is sampling with 1 s energy sweeps.

335

3.2. Photoelectron Peaks Observed in the Martian Ionosphere

The spacecraft enters the ionosphere from the night side of the planet and observes peaks in the photoelectron spectrum beginning at about 1535 UT (625 km altitude) until it exits into the dayside magnetosheath around 1558 UT (725 km altitude). A more detailed view can be obtained by examining the combined ion and electron spectrogram. Figure 4 shows the ion spectrogram measured by IMA sector 0 (IMA-00) in the top panel and the electron spectrogram measured by ELS sector 4 (ELS-04) in the bottom panel. At this time, IMA is observing low-energy ions in its fast sample rate mode (96 energy measurements from 10 eV to 30 keV in 12 sec); its elevation analyzer is not stepping. ELS is also measuring in its fast sample rate mode (31 energy measurements from 9 eV to 150 eV in 1 sec) and the ASPERA-3 scanner is parked. This condition also generates a 2D ELS measurement.

[Figure 4]

Overlaid on the ion spectrogram is the integral electron flux from the observed electrons with energies between 5 eV and 100 eV. Overlaid on the electron spectrogram is the spacecraft altitude (in km), indicating that the pericenter is reached at about 1545 UT. The solar zenith angle (SZA), planetodetic latitude (PdLat), planetodetic longitude (PdLon), solar time (SolTime), and solar latitude (SolLat) of the spacecraft are shown along the bottom axis and

given every 6 minutes.

355 In Figure 4, the photoionization peaks observed in the electron spectrogram from carbon
dioxide and atomic oxygen are seen in the ionosphere at the same time that low-energy ions are
observed. The peaks in the electron spectrogram are observed to decrease in energy with
decreasing altitude, and at the same time the trace in ion flux increases in energy. This behavior
means that during this pass, the spacecraft was charging negatively, forcing the detected
360 electrons to decelerate and lose kinetic energy as they fall to the spacecraft. At the same time,
the ions are accelerated as they fall through the potential well created by the spacecraft charge.
The amount of spacecraft charging becomes a larger negative value as the spacecraft altitude
approaches the pericenter altitude, about 290 km, indicated by a change in the energy location of
the peaks from photoionization of carbon dioxide and atomic oxygen.

365 At about 1535 UT dayside ionospheric electrons begin to be observed on the
spectrogram, the integral electron flux (which had been decreasing) shows a sudden increase,
and the ion flux intensity also shows a sudden increase. This increase marks the location of the
photoelectron boundary (PEB).

 In the ionosphere, peaks in the photoelectron spectrum are nearly isotropic. At the same
370 time, ions are anisotropic. Each spacecraft pass shows a different amount of detected ions and a
different degree of anisotropy; however, in this paper we are focusing on the electrons and the
electrons shown here are fluxes representative of the ionosphere.

 A detailed examination of the electron spectrum from the ionosphere is shown in
Figure 5. Presented is the differential energy flux spectrum of ELS sector 4 averaged between
375 15:43:59 UT through 15:45:08 UT. Because ELS is measuring an energy spectrum every second
at this time, about 50 spectral measurements are averaged. The region below about 60 eV

mainly comes from photonic inputs. The peaks in energy due to the photoionization process appear between about 10 and 13 eV, and at about 16 eV. The locations of the energy peaks are shifted in energy due to the spacecraft potential. During the time period in which this data was
380 collected, the spacecraft potential is nearly constant at about -10.8 volts. It is important to note that despite the energy shift, the photoelectron peaks remain a relatively sharp feature of the spectrum showing a two peak structure in the data.

[Figure 5]

Error bars are also shown on this plot and include (1) Poisson statistics, (2) telemetry
385 compression uncertainties, and (3) instrument uncertainties. Instrument uncertainties include uncertainties derived from the (1) physical geometric factor, (2) microchannel plate transparency, (3) protection grid transparency, (4) active anode area ratio, (5) accumulation time, (6) energy resolution, (7) relative microchannel plate efficiency, and (8) detection efficiency (Bordoni, 1971).

390

3.3. Photoelectron Peaks Observed in the Martian tail

The orbit of the spacecraft causes it to exit the dayside of the ionosphere, pass through the bow shock, and enter the solar wind before reentering the magnetosheath on the night side in
395 the deep tail (10,000 km altitude). The section of the orbit in the tail encompassing the inner magnetospheric boundary is presented in Figure 6. In this figure, the spacecraft data begins in the magnetosheath (1931 UT) at an altitude of about 10,000 km and concludes (2031 UT) in the Martian tail at an altitude of about 8,400 km. The format of Figure 6 is in the same as Figure 4.

[Figure 6]

400 The IMA data shows that there is solar wind penetration into the magnetosheath from the
beginning of the plot to about 1946 UT. Examining the orbit plot (Figure 3), it is seen that the
position of the inner magnetospheric boundary is closer to the MSO X-axis than the average
position of the magnetic pile-up boundary of Vignes et al. (2000). This indicates that the
Martian magnetosphere is slightly compressed from the average position. At the IMB, the
405 integral electron flux (top panel) shows a decrease in intensity inside the Martian tail compared
with that in the magnetosheath.

The electrons in the magnetosheath show oscillations in the flux, resembling a series of
closely bunched electron beams. Just after the IMB is crossed, there is a decrease in the electron
flux and then a slight increase between about 1956 UT and 2014 UT (about 9,600 - 9,000 km
410 altitude). The flux increases again between about 2018 UT and 2024 UT (about 8,900 -
8,700 km) before again decreasing in intensity. Between about 2018 UT and 2024 UT,
photoelectron peaks are observed in the electron energy spectrum which are termed "distinct",
and between about 1956 UT and 2014 UT, one peak is observed and termed "degraded". These
are discussed in more detail below.

415

3.3.1. Distinct Photoelectron Peaks

Figure 7 shows distinct photoelectron peaks observed in the Martian tail for ELS
sector 4. The format is similar to that of Figure 5. In this case, ELS sector 4 is viewing nearly
420 parallel to the IMB, toward the Sun, and toward Mars. Presented is the differential energy flux
spectrum averaged between 20:22:59 UT through 20:24:08 UT, so again about 50 spectral
measurements are averaged. Comparison of this tail spectrum with that measured in the

ionosphere shows similarity below 60 eV, which implies that ionospheric plasma is flowing away from the planet. In particular, the photoelectron peaks of carbon dioxide and atomic oxygen are created near the exobase on the day side of the planet where the densities are large enough to generate distinct electron peaks in the energy spectrum, so spectra showing these distinct photoelectron features must come from the dayside.

[Figure 7]

Again for this spectrum, there is a dual peak structure observed. The peaks in energy due to the photoionization process appear between about 15 and 18 eV, and at about 21 eV. The location of the energy peaks are shifted in energy due to the spacecraft charge (see the discussion of the effects of spacecraft potential in section 4). During the time period where this data was collected, the spacecraft potential is nearly constant at about -5.6 volts. It is important to note that despite the energy shift and the flow from the dayside, the photoelectron peaks remain a relatively sharp feature of the spectrum showing a two peak structure in the data.

3.3.2. Degraded Photoelectron Peaks

Some measurements in the Martian tail exhibit electron spectra in which the peaks in energy are not distinct. For these cases, the two peak structure of the carbon dioxide and atomic oxygen photoelectrons is merged into one broad peak, showing energy degradation. This spectrum is shown in Figure 8 for ELS sector 4. The format is similar to that of Figure 5. In this case, ELS sector 4 is viewing in nearly the same direction as when distinct photoelectron peaks are observed. Presented is the differential energy flux spectrum averaged between 20:01:59 UT and 20:03:08 UT; as before about 50 spectral measurements are averaged.

[Figure 8]

Comparison of the degraded tail spectrum (Figure 8) with the spectrum showing distinct photoelectron peaks (Figure 7) suggests that the spacecraft is charged to about the same potential in each case, -5.6 V. This assessment is made based on the observation that (a) the flux above 450 50 eV is similar for the two spectra, and (b) shoulders of the photoelectron populations in the two spectra (the ~40-50 eV range) begin to intensify at the same energy (near 50 eV). Below 50 eV the flux of the degraded spectrum is lower than that of the spectrum with distinct peaks, and the energy peaks are shifted toward lower energies by about 8% (one ELS energy channel width), presumably as a result of process(es) responsible for the degradation. The degradation 455 may be the result of the distribution becoming so field aligned that it leads to an instability which diffuses the distribution in phase space. Our observation that not all spectra are degraded may be an indication that some field lines emerge from regions of strong crustal field whereas others emerge from very weak-field regions. Although beyond the scope of this paper, the observations suggest a way to improve our knowledge of particle transport along magnetic field 460 lines in the Mars environment.

In the spectrogram shown in Figure 6, the region showing the degraded photoelectron peaks in the spectrum is closer to the IMB than spectra showing distinct photoelectron peaks, with the spectra showing degraded peaks occurring at higher altitudes (between about 1956 UT and 2014 UT, about 9,600 - 9,000 km altitude) than spectra showing distinct peaks (between 465 about 2018 UT and 2024 UT, about 8,900 - 8,700 km). Statistics accumulated to date and reported in Frahm et al. (2006b) do not include a contribution from spectra showing degraded peaks, since they would not have been recognized as producing either a dual peak structure (as in Figure 1) or a well defined lower energy peak with a hint at larger flux at the location of the

higher energy peak (as in Figure 2) in the energy spectrum. Thus, the rates calculated from our
470 statistics will under represent the actual loss.

4. Effect of Spacecraft Charging

Toward the end of the Figure 6 spectrogram (near 2024 UT), low-energy ions are
475 observed. These low-energy ions appear just above the low-energy threshold of IMA.
Spacecraft potential is -5.6 volts in the tail when the distinct photoelectron peaks are observed,
but is -10.8 volts in the ionosphere. This means that for low-energy ions initially of the same
energy, the ions accelerated by the spacecraft potential would be detected by IMA at greater
energies in the ionosphere than in the tail. The spacecraft potential is highly variable, and can
480 change in magnitude and polarity within a few seconds. As can be seen in Figure 6, when the
low-energy ions appear, the electron flux decreases. In this region, the strong dayside
atmospheric electron signature disappears and the clue to the level of spacecraft potential
vanishes. Thus, the charge on the spacecraft in this region is unknown and could very well be
more negative so that low-energy ions (which would normally be below the IMA energy
485 threshold) appear. Typically, the MEx spacecraft charges positively in the Martian
magnetosheath and negatively below the IMB. Thus, the spacecraft charging level varies
through out the orbit and it is possible that the charge on the spacecraft changed enough that
low-energy ions are observed.

The effect of spacecraft charging can be removed from the spectra if the spacecraft
490 potential is known. For electrons, it is possible for a positive spacecraft potential to be estimated
when the ambient plasma electrons are detected (Johnstone et al., 1997). In general, when the

spacecraft is negatively charged, determination of a feature in the electron spectrum which allows the spacecraft potential to be estimated, cannot be found. Fortunately measurement of the photoelectron peaks provides an opportunity to estimate a negative spacecraft potential.

495 Estimates of the spacecraft potential are determined from the difference between the measured peak value and the theoretical location of that value.

The electron spectrum in the ionosphere shown in Figure 5, corrected with an estimated spacecraft potential of -10.8 volts, is shown in Figure 9. The estimated value is generated after averaging has been completed. Similarly, the electron spectrum showing distinct photoelectron
500 peaks in the Martian tail (Figure 7), corrected with an estimated spacecraft charge of -5.6 volts is shown in Figure 10, and the corrected degraded tail spectrum (Figure 8) is shown in Figure 11. Estimates of spacecraft potential are good to within an energy channel width since it can not be determined where in the channel the peak actually lies. For the ionosphere, the uncertainty of the spacecraft potential is ± 0.7 volts; for the tail, the uncertainty is ± 0.9 volts.

505 **[Figure 9, Figure 10, Figure 11]**

Correcting the differential energy flux for the spacecraft potential (Φ) is accomplished by shifting the electron distribution function to the new energy (E'), given by $E' = E - \Phi$. To obtain the corrected differential energy flux, it is necessary to convert the distribution function, shift the energy, then convert back to differential energy flux (DEF), resulting in the following
510 expression for the corrected flux $DEF(E') = DEF(E) \cdot (E'/E)^2$.

Another possible contributing factor to the value of Φ is a field-aligned potential drop from the dayside ionosphere to the observation location in the magnetotail. Liemohn et al. (1997) calculated such potential drops for photoelectrons in the Earth's magnetosphere, finding a value of a few volts along inner magnetospheric field lines undergoing plasmaspheric refilling.

515 Such a ambipolar potential drop might also exist for these high-altitude photoelectrons in Mars
tail. Therefore, the actual spacecraft potential might be closer to zero during this time. This
additional contributor to Φ , however, does not change the results of the escape rate analysis
below, in which the spectrum has been shifted by the total value of Φ , regardless of its origin.

520 **5. Electron Outflow**

The electron outflow can be estimated by using previously collected statistics on the
occurrence frequency of spectra showing photoelectron peaks (Frahm et al., 2006b), along with
the number of photoelectrons generated in the region of the peaks and an estimate of the area
525 through which the photoelectrons pass on their escape down the Martian tail. In addition, the
angular extent of measured spectra showing photoelectron will be considered.

5.1 Tail Photoelectron Peak Frequency

530 The MEx ELS was used to gather occurrence frequencies of the observation of peaks in
the photoelectrons primarily caused by the dayside atmospheric ionization of carbon dioxide and
atomic oxygen (Frahm et al., 2006b). These statistics were generated for all those measurements
which showed discrete photoelectron peaks (similar to those shown in Figures 6 and 7) between
5 January 2004 and 13 November 2004. Extending the sample collection period to 25 January
535 2005, the updated frequency of occurrence statistics is shown in Figure 12. These data are
presented in cylindrical MSO coordinates with the Sun at the right, tracing the orbit of the MEx
spacecraft in a format similar to Figure 3. For these data, all locations of MEx when ELS

measured spectra are shown in Figure 12b (color coded by the number of samples of the electron spectrum made by ELS), while in Figure 12a, only those spectra showing distinct photoelectron spectra in ELS sector 3 are included (color coded by the fraction of spectra which showed distinct photoelectron peaks).

[Figure 12]

During this survey, spectra showing a degraded photoelectron peak (similar to that shown in Figure 8) would not have been recognized as the type of spectra to mark as photoelectron peak spectra in this study and would have been included as measurements not showing photoelectron peaks. This should reduce the occurrence frequency of photoelectron peaked spectra. At the present time, there is no assessment of how inclusion of degraded spectra would change the statistics shown in Figure 12.

The statistics gathered in Figure 12 are only for ELS sector 3, which in general exhibited the strongest signal during 2004; however, this was not always the case. ELS sector 3 generally pointed toward the planet in the tail of Mars and rotated to point in the direction of the planet on its dayside. ELS sector 3 occasionally pointed at various other angles. When this occurred, only ELS sector 3 was monitored and a photoelectron peak spectrum was recorded if ELS sector 3 showed the appropriate signal. If additional ELS sectors had been examined, they might have detected more photoelectron peak spectra and the ratios in Figure 12a would be increased. At the present time, there is no assessment of how statistics shown in Figure 12 would change if other ELS sectors were included in the survey. In addition, MEx is only at one location at a time and ELS can only determine whether photoelectron peaks are observed at the current MEx location. ELS can not determine if the escape of the photoelectron peaked plasma is spatially dependent.

An estimate of the total fraction of spectra showing distinct photoelectron peaks from ELS sector 3 can be generated by counting all spectra showing distinct photoelectron peaks tailward of $1.5 R_{\text{Mars}}$ ($R_{\text{Mars}} = 3393 \text{ km}$) and within (closer to the symmetry axis line than) the averaged MPB determined by Vignes et al. (2000). For the statistics gathered in Figure 12, there are 241,490 spectra measured by ELS sector 3 tailward of $X = -1.5 R_{\text{Mars}}$. Of these, there are 14,951 spectra measured by ELS sector 3 tailward of $X = -1.5 R_{\text{Mars}}$ which measured distinct photoelectron peaks. Thus, in 2004, ELS measured distinct photoelectron peak spectra for 6.2% of the time.

5.2 Line Width and Background Photon Population

The solar spectrum at and in the neighborhood of 30.4 nm (40.79 eV) can be found in Gibson (1973). The line width of the 30.4 nm HeII line is about 0.1 nm. Translating this into an energy width of the detected electrons produced by the photoionization process gives an uncertainty in the electron energy of about $\pm 0.07 \text{ eV}$. Since the energy channel width of ELS is about 8.3%, at 10 eV, 20 eV, and 30 eV the widths of the ELS energy channels are about 0.8 eV, 1.7 eV, and 2.5 eV, respectively. Thus, the expected width of the photoelectrons generated from the photoionization process just due to the spread in the 30.4 nm photons is small with respect to the energy channel width of the ELS instrument. We should expect to observe a sharp amplitude increase for those energy channels which contain the photoionized electrons (distinct) as opposed to a gradual increase in ELS data lasting over several measured energy channels.

It is also noticed from Gibson that the 30.4 nm HeII line rides on top of a continuous background of photons in the $10^{13} \text{ photons}/(\text{cm}^2 \text{ s sr})$ range. These background photons with

energies above the ionization potential for carbon dioxide and atomic oxygen could also
585 photoionize and create a small amount of background photoelectrons; however, the dominant
source of photoionization from carbon dioxide and atomic oxygen is the 30.4 nm HeII line
which extends at least an order of magnitude above the background solar photons. Thus,
without the 30.4 nm HeII line present, we should expect to observe background photoelectrons
at energies where the photoionization peaks occur.

590

5.3. Number of Electrons Emitted From Photoionization

The number of electrons within the photoelectron peaks generated by the HeII 30.4 nm
line, represented by the distinct tail spectrum of Figure 10, can be estimated through integration
595 of the spectrum. A blow-up of the region which shows photoelectron peaks, converted to
differential number flux, is shown in Figure 13. Each datum is labeled with a reference number,
0 to 8. In order to estimate the number of photoelectrons generated by the HeII 30.4 nm line, we
use the knowledge of background photons to draw a continuous line between points 1 and 7 in
log space, determine the differential number flux (DNF) values along this line for the
600 intervening points ($DEF(E') = E' \cdot DNF(E')$), and then find the number intensity beneath the linear
line. This we will take as the background spectrum which would be generated if the solar HeII
30.4 nm line was not present. This area is 9.04×10^6 electrons/($\text{cm}^2 \text{ s sr}$).

[Figure 13]

The contribution due to both the background and the contribution of the HeII 30.4 nm
605 line is determined by integrating the points 1-7 on the spacecraft charge adjusted spectrum. This
area is 1.48×10^7 electrons/($\text{cm}^2 \text{ s sr}$). Thus, the portion of the number intensity which is due to

the presence of the HeII 30.4 nm line is just the difference, or 5.74×10^6 electrons/($\text{cm}^2 \text{ s sr}$).

The uncertainty in the number of electrons generated by the HeII 30.4 nm line is estimated by determining the maximum and minimum area differences. During this process, the requirement

610 when making integration estimates is that both the background and background plus HeII
30.4 nm line contribution begin at the same offsets for points 1 and 7. Then, the minimum
(maximum) difference is determined using the same scheme as described above except the
background line is figured by drawing the line between point 1's maximum (minimum)
uncertainty value and point 7's maximum (minimum) uncertainty. The background plus HeII
615 30.4 nm line contribution is determined by using the same values for points 1 and 7, while on
points 2-6, using the minimum (maximum) uncertainty value. Thus, the minimum (maximum)
difference is 4.48×10^6 (7.00×10^6) electrons/($\text{cm}^2 \text{ s sr}$). Combining all of our estimates, the
number of electrons generated by the presence of the HeII 30.4 nm line due to ionization of
carbon dioxide and atomic oxygen is $5.74 \times 10^6 \pm 1.26 \times 10^6$ electrons/($\text{cm}^2 \text{ s sr}$).

620

5.4. 2004 Spectral Intensity

Since the calculation just performed was made using our illustrative example pass, it is appropriate to question how accurately the resulting flux value represents the “average”

625 observation of photoelectrons in the Mars outflow region (i.e., essentially, the magnetospheric
tail). To answer this question we have examined in detail a subset of 22 cases of photoelectron
observations made during the observation time period (5 January 2004 through 25 January
2005). These cases were selected based on two criteria: (1) they had to exhibit distinct
photoelectron peaks, over which a good average spectrum could be obtained, and (2) they had to

630 span the region between $X \leq -1.5 R_{\text{Mars}}$ and the maximum distance of MEx downtail,
X $\sim -3.7 R_{\text{Mars}}$. With each observation, a spectral average was calculated, the spacecraft potential
determined, and the electron flux generated by the HeII 30.4 nm line due to ionization of carbon
dioxide and atomic oxygen was determined (as was described above for the illustrative example
spectrum). The electron intensities for each case, the average electron intensity, and the standard
635 deviation are shown in Table 2 and Figure 14.

[Table 2, Figure 14]

Figure 14 shows the integrated number intensity for each averaged spectrum as a
function of sequence number and the approximated uncertainty using the method described in
the previous section. The sequence number is a rough approximation to a UT time scale. The
640 average flux of this data set is 4.15×10^6 electrons/(cm² s sr) with a standard deviation of
 6.70×10^5 electrons/(cm² s sr), also shown on Figure 14. Even though the flux value of the
illustrative case falls within the set of flux values of Table 2 and also illustrated by Figure 14, it
lies slightly more than one standard deviation from the mean value. Accordingly, we use the
average value as representative of fluxes in the outflow region. Thus, we adopt this average
645 value of electron intensity, $4.15 \times 10^6 \pm 6.70 \times 10^5$ electrons/(cm² s sr), as the average number of
electrons generated by the presence of the HeII 30.4 nm line due to ionization of carbon dioxide
and atomic oxygen.

Examination of the data included within Table 2 shows there are two main time intervals
when peaks in the photoelectron spectra are selected for this study. These two time regions of
650 data are caused by both our selection criteria and the MEx orbit. Examination of Figure 14 does
not show a large enough difference in the integrated number intensity values to infer that the flux
is controlled by either EUV or solar wind forcing as illustrated in the ion escape by Lundin et al.

(2008a), nor is there sufficient cause to suspect any difference in escape rates based on the MSO-X detection position as illustrated in the ions by Lundin et al. (2008b).

655

5.5. Angular Measurement Range

The number of ELS sectors which show the photoelectron peaks is dependent on the orientation of MEx and ELS, as well as the angular distribution of electrons. To make an estimate of the solid angle characterizing the electron angular distribution, we have recorded the number of sectors containing photoelectron peaks for each of the 22 cases shown in Table 2. The results appear in the right most column of the table, where it is seen that photoelectron peaks were measured in as few as 2 and as many as 5 sectors (these measurements are consistent with results from ELS observations, modeling, and simulations of Liemohn et al. (2006a)). For our estimate we take the average value of 3 sectors, measuring from 67.5° , which is assumed to be the full angle of a conical distribution. Thus at half maximum, the value of the solid angle is 33.75° .

So, being conservative, we use the solid angle of a cone which includes three ELS sectors, with the radii of the cone of 33.75° , corresponding to the angular width of one and a half ELS sectors. This angular area for three filled sectors is 1.059 sr. Here we will take the uncertainty in angle of half an angular channel width, or 11.25° , giving an angular area of coverage of 1.059 ± 0.575 sr. This gives an escaping number flux of $4.39 \times 10^6 \pm 2.49 \times 10^6$ electrons/(cm^2 s) due to the ionization of carbon dioxide and atomic oxygen. Since we know that in 2004, escape occurred 6.2% of the time, an estimate of the average loss of electrons during 2004 from ionization caused by the solar HeII line is $2.72 \times 10^5 \pm 1.54 \times 10^5$

electrons/(cm² s).

Included within this angular estimation are the assumptions that 1) the electron distribution is gyrotropic and 2) the angular extent of the measurement includes the entire pitch angle distribution. Since electrons are almost always cylindrically symmetric about the magnetic field, gyrotropy is reasonable. The assumption of angular extent of the measurement can not be confirmed since MEx contains no magnetometer; there is no satisfactory means of determining the local pitch angle distribution without a direct measurement of the magnetic field. Thus, the assumption was necessary. If however, ELS does not measure the full angular extent of the pitch angle distribution, then the escape rates would be an under estimate because a portion of the angular distribution would be missing from the estimate.

5.6. Tail Area Outflow

The surface area through which electrons escape Mars covers only the region measured by MEx. In three-dimensional space, there are locations which were not measured (see Frahm et al., 1996b). For this reason, we collapse the ELS measurements into the two-dimensional plane and estimate the outflow as if the outflow were symmetric. The count statistics are considered to reflect both a spatial and temporal frequency of occurrence rates.

Even in two-dimensions, not all locations were measured in the tail of Mars during 2004. Estimating the MSO radius which contained measurements, the location of MEx in the tail shown in Figure 12 was projected on to the $X_{\text{MSO}} = -1.5 R_{\text{Mars}}$ surface, which was determined to be $R_{\text{minimum}} = 2850$ km. Due to the density of measurements, samples were found to occur within the radius of the average MPB position at $X_{\text{MSO}} = -1.5 R_{\text{Mars}}$, a radial distance of $R_{\text{maximum}} =$

6700 km. This gives an estimated annular area of $1.16 \times 10^{18} \text{ cm}^2$ which allows an estimation of
700 the escape rate of the photoionized electrons at $3.14 \times 10^{23} \pm 1.78 \times 10^{23}$ electrons/s. Now 2004
contained about 3.17×10^7 s, which gives about $9.92 \times 10^{30} \pm 5.62 \times 10^{30}$ electrons that escape
Mars. Since Avogadro's number is 6.022×10^{23} particles/mole, this represents a loss of about
 16.5 ± 9 Mmole of electrons lost from the atmosphere of Mars just in the photoionization of
carbon dioxide and atomic oxygen from the solar HeII 30.4 nm line.

705

6. Caveats to Electron Outflow Determination

This outflow of electrons included within the photoelectron peaks at Mars should be
taken as an estimate. A more rigorous way to estimate the electron escape from Mars would be
710 to add up the contribution from each ELS spectrum, taking into account the individual amplitude
of the flux, angular extent of the flux, and correcting individual spectra for the charge on the
spacecraft; however, this would require more resources than currently available and is not
possible at this time. In addition, since MEx contains no magnetometer, an assumption is
applied to each measurement that the angular measured flux is representative of the entire pitch
715 angle distribution. Although with instrumental and calculational uncertainties the angular extent
determined from Table 2 ($\sim 34^\circ$) is less than that predicted by Liemohn et al. (2006a).

The statistics gathered (Frahm et al., 2006b) only indicate whether or not ELS sector 3
shows distinct photoelectron peaks. The spectra in that survey are not corrected for spacecraft
charge; however, spectra averaged in Table 2 and used for this estimation are individually
720 corrected for the potential on the spacecraft. At times, spectra exhibiting distinct photoelectron
peaks are missed by this survey because they occur in different ELS sectors than sector 3. In

most cases within 2004, the orientation of the spacecraft and the ELS observation plane in the Martian tail was parallel to the Mars-Sun line. Spacecraft rotations occurred as the spacecraft neared the planet which could cause ELS sector 3 to swing out of this orientation, and moving
725 the signal of the distinct photoelectron peaks into other ELS sectors. The influence of spacecraft rotations on the occurrence frequency of high-altitude photoelectron observations was noted by Liemohn et al. (2006b), who compared computed magnetic field line connectivity with the ELS photoelectron statistics of Frahm et al. (2006b). At rare times in the Martian tail, a signal which appears to be a degraded photoelectron peak can be observed flowing toward the planet;
730 however, due to the orientation of the MEx spacecraft, the ELS signal is not clear, as the parent electron population is influenced by scatter and secondaries from the spacecraft.

6.1. Location of measurements

735 Statistics based on the 2004 data are biased toward the flanks of the Martian magnetosphere (Frahm et al., 2006b). There was no ELS data taken over the Martian poles during 2004 due to orbital constraints and operational limits. Because of this, estimates could be substantially off. At the present time, the occurrence rates over the poles are unknown. However, Liemohn et al. (2006b) determined the connectivity between the polar tail regions and
740 the dayside ionosphere from numerical simulations, showing very little high-latitude connectivity far from the planet.

The region of escape of photoelectron peaks from the atmosphere is mostly between the ionosphere and the MPB near the planet toward the nightside. This flux expands into the tail, but the collected statistics indicate that photoelectrons from the atmosphere are not observed in

745 the shadow region of the tail.

6.2. Degraded Photoelectron Peak Spectra

Although the statistics in Figure 12 do not include spectra showing degraded
750 photoelectron peaks, a few may be contained within statistics. These would be spectra which
suggest a flat energy dependence of the ground state ionization, similar to Figure 2. This could
occur because of low counting statistics causing a suggestion of a primary peak. In these cases,
it would have been assumed that spacecraft charging had shifted the spectra to lower energies,
which has a tendency to broaden the lower energy peak. However, spectra which did not show a
755 flat region prior to the broader lower energy peak would have been excluded from this survey.

7. Conclusion

A MEx orbit showing photoelectron peaks caused by the He 30.4 nm photoionization of
760 carbon dioxide and atomic oxygen is shown as representative of cases where these photoelectron
peaks appear in the ELS data. The particular pass chosen shows distinct photoelectron peaks in
the ionosphere, degraded photoelectron peaks in the tail close to the IMB, and distinct
photoelectron peaks at lower altitudes in the Martian tail. Consideration of energy offsets from
theoretical values of distinct peaks in the ionosphere as well as the tail can provide an estimate
765 of the potential of the spacecraft. For peaks in the ionosphere of this orbit, the spacecraft charge
level changes with altitude, but is fairly steady in the Martian tail where photoelectron peaks are
observed. Estimation of the spacecraft potential allows correction of the electron spectrum.

An average integrated number intensity, determined from a subset of the full set of data, is taken to represent the sampled discrete photoelectron spectra from the Martian tail in 2004.

770 This was used to calculate the number of electrons escaping the planet from the ionization process, computed to be $4.39 \times 10^6 \pm 2.49 \times 10^6$ electrons/(cm² s). Statistics gathered on the occurrence frequency of the spectra show that these photoelectron peaks occur about 6.2% of the time during 2004. Thus the outflow of electrons is estimated to be $2.72 \times 10^5 \pm 1.54 \times 10^5$ electrons/(cm² s) during 2004. An estimate of the outflow area, 1.16×10^{18} cm², allows
775 estimation of the electron escape rate of $3.14 \times 10^{23} \pm 1.78 \times 10^{23}$ electrons/s caused by the ionization of carbon dioxide and atomic oxygen by the HeII 30.4 nm line during 2004. This can be expressed as the total number of electrons that escape in 2004 as about $9.92 \times 10^{30} \pm 5.62 \times 10^{30}$ electrons or about 16.5 ± 9 Mmole of electrons lost from the atmosphere of Mars in the photoionization of carbon dioxide and atomic oxygen caused by the solar HeII 30.4 nm line.
780 Due to the caveats of the analysis, these derived escape rates should be considered lower limits on the total electron escape rate from Mars.

The ion escape rate reported by Barabash et al. (2007) using 2004-2006 ion data determine an O⁺ loss rate of 1.6×10^{23} s⁻¹, an O₂⁺ loss rate of 1.5×10^{23} s⁻¹, and a CO₂⁺ loss rate of 8×10^{22} s⁻¹, which gives a total loss rate of 3.9×10^{23} s⁻¹. These correspond to byproducts of the
785 described carbon dioxide and atomic oxygen photoionization in equations 1 and 2. The result of these ion loss rates are within our estimated uncertainty for electron escape; however, they represent an order of magnitude less than the ion escape rates determined by Lundin et al. (2008a,b) using 2007-2008 ion data.

790 **Acknowledgments**

The ASPERA-3 experiment on the European Space Agency (ESA) Mars Express mission is a joint effort between 15 laboratories in 10 countries, all sponsored by their national agencies.

We thank all these agencies as well as the various departments/institutes hosting these efforts.

795 We wish to acknowledge support through the National Aeronautics and Space Administration (NASA) contract NASW-00003 in the United States, Particle Physics and Astronomy Research Council (PPARC) in the United Kingdom, and wish to thank those NASA officials who had the foresight to allow augmentation of the original ASPERA-3 proposal for ELS so that it would provide the additional capabilities which allowed the science described in this paper to be
800 conducted. We also wish to acknowledge the Swedish National Space Board for their support of the main PI-institute and we are indebted to ESA for their courage in embarking on the Mars Express program, the first ESA mission to the red planet. In addition, we would like to thank C. A. Gonzalez, S. J. Jeffers, J. Mukherjee, M. Muller, and J. R. Scherrer at SwRI for their extensive work on and with ASPERA-3.

805

References

810 Acuña, M. H., Connerney, J. E. P., Wasilewski, P., Lin, R. P., Anderson, K. A., Carlson, C. W., McFadden, J., Curtis, D. W., Mitchell, D., Rème, H., Mazelle, C., Sauvaud, J.-A., d'Uston, C., Cros, A., Medale, J. L., Bauer, S. J., Cloutier, P., Mayhew, M., Winterhalter, D., Ness, N. F. 1998. Magnetic field and plasma observations at Mars: Initial results of the Mars Global Surveyor mission. *Science*, 279, 1676-1680.

815 Barabash, S., Lundin, R., Andersson, H., Gimholt, J., Holmström, M., Norberg, O., Yamauchi, M., Asamura, K., Coates, A. J., Linder, D. R., Kataria, D. O., Curtis, C. C., Hsieh, K. C., Sandel, B. R., Fedorov, A., Grigoriev, A., Budnik, E., Grande, M., Carter, M., Reading, D. H., Koskinen, H., Kallio, E., Riihelä, P., Säles, T., Kozyra, J., Krupp, N., Livi, S., Woch, J., Luhmann, J., McKenna-Lawlor, S., Orsini, S., Cerulli-Lrelli, R., Maggi, M., Morbidini, A., Mura, A., Milillo, A., Roelof, E., Williams, D., Sauvaud, J.-A., Thocaven, J.-J., Moreau, T., Winningham, D., Frahm, R., Scherrer, J., Sharber, J., Wurz, P.,
820 Bochsler, P. 2004. ASPERA-3: Analyser of Space Plasmas and Energetic Ions for Mars

Express. In: Wilson, A. (Ed), Mars Express: The Scientific Payload. European Space Agency Publications Division, European Space Research & Technology Centre, Noordwijk, The Netherlands, SP-1240, 121-139.

825

Barabash, S., Lundin, R., Andersson, H., Brinkfeldt, K., Grigoriev, A., Gunell, H., Holmström, M., Yamauchi, M., Asamura, K., Bochsler, P., Wurz, P., Cerulli-Irelli, R., Mura, A., Milillo, A., Maggi, M., Orsini, S., Coates, A. J., Linder, D. R., Kataria, D. O., Curtis, C. C., Hsieh, K. C., Sandel, B. R., Frahm, R. A., Sharber, J. R., Winningham, J. D., Grande, M., Kallio, E., Koskinen, H., Riihelä, P., Schmidt, W., Säles, T., Kozyra, J. U., Krupp, N., Woch, J., Livi, S., Luhmann, J. G., McKenna-Lawlor, S., Roelof, E. C., Williams, D. J., Sauvaud, J.-A., Fedorov, A., Thocaven, J.-J. 2006. The Analyzer of Space Plasmas and Energetic Atoms (ASPERA-3) for the Mars Express Mission. *Space Sci. Rev.*, 126, 113-164.

835

Barabash, S., Fedorov, A., Lundin, R., Sauvaud, J.-A. 2007. Martian atmospheric erosion rates. *Science*, 315, 501-503.

840

Bordoni, F. 1971. Channel electron multiplier efficiency for 10-1000 eV electrons. *Nucl. Instrum. Methods*, 97, 405-408.

845

Carlsson, E., Fedorov, A., Barabash, S., Budnik, E., Grigoriev, A., Gunnell, H., Nilsson, H., Sauvaud, J.-A., Lundin, R., Futaana, Y., Holmström, M., Andersson, H., Yamauchi, M., Winningham, J. D., Frahm, R. A., Sharber, J. R., Scherrer, J., Coates, A. J., Linder, D. R., Kataria, D. O., Kallio, E., Koskinen, H., Säles, T., Riihelä, P., Schmidt, W., Kozyra, J., Luhmann, J., Roelof, E., Williams, D., Livi, S., Curtis, C. C., Hsieh, K. C., Sandel, B. R., Grande, M., Carter, M., Thocaven, J.-J., McKenna-Lawler, S., Orsini, S., Cerulli-Irelli, R., Maggi, M., Wurz, P., Bochsler, P., Krupp, N., Woch, J., Fränz, M., Asamura, A., Dierker, C. 2006. Mass composition of the escaping plasma at Mars. *Icarus*, 182, 320-328, doi:10.1016/j.icarus.2005.09.020.

850

Dubinin, E. Fränz, M., Woch, J., Roussos, E., Barabash, S., Lundin, R., Winningham, J. D., Frahm, R. A., Acuña, M. 2006. Plasma morphology at Mars. ASPERA-3 observations. *Space Sci. Rev.*, 126, 209-238, doi:10.1007/s11214-006-9039-4.

855

Duru, F., Gurnett, D. A., Winningham, J. D., Frahm, R., Modolo, R. this issue. A flow velocity boundary in the upper ionosphere of Mars from the disappearance of electron plasma oscillations. *Icarus*.

860

Fox, J. L., Dalgarno, A. 1979. Ionization, luminosity, and heating of the upper atmosphere of Mars. *J. Geophys. Res.*, 84, 7315-7333.

865

Frahm, R. A., Winningham, J. D., Sharber, J. R., Scherrer, J. R., Jeffers, S. J., Coates, A. J., Linder, D. R., Kataria, D. O., Lundin, R., Barabash, S., Holmström, M., Andersson, H., Yamauchi, M., Grigoriev, A., Kallio, E., Säles, T., Riihelä, P., Schmidt, W., Koskinen, H., Kozyra, J. U., Luhmann, J. G., Roelof, E. C., Williams, D. J., Livi, S., Curtis, C. C., Hsieh, K. C., Sandel, B. R., Grande, M., Carter, M., Sauvaud, J.-A., Fedorov, A.,

- 870 Thocaven, J.-J., McKenna-Lawler, S., Orsini, S., Cerulli-Irelli, R., Maggi, M., Wurz, P.,
Bochsler, P., Krupp, N., Woch, J., Franz, M., Asamura, K., Dierker, C. 2006a. Carbon
dioxide photoelectron energy peaks at Mars. *Icarus*, 182, 371-382.
- 875 Frahm, R. A., Sharber, J. R., Winningham, J. D., Wurz, P., Liemohn, M. W., Kallio, E.,
Yamauchi, M., Lundin, R., Barabash, S., Coates, A. J., Linder, D. R., Kozyra, J. U.,
Holmström, M., Jeffers, S. J., Andersson, H., Mckenna-Lawler, S. 2006b. Locations of
atmospheric photoelectron energy peaks within the Mars environment, *Space Sci. Rev.*,
126, 389-402, doi:10.1007/s11214-006-9119-5.
- 880 Gibson, E. G. 1973. *The Quiet Sun*, NASA SP-303, National Aeronautics and Space
Administration, Washington, D.C.
- 885 Johnstone, A. D., Alsop, C., Burge, S., Carter, P. J., Coates, A. J., Coker, A. J., Fazakerley, A. N.,
Grande, M., Gowen, R. A., Gurgiolo, C., Hancock, B. K., Narheim, B., Preece, A.,
Sheather, P. H., Winningham, J. D., Woodliffe, R. D. 1997. PEACE: A Plasma Electron
And Current Experiment. *Space Sci. Rev.*, 79, 351-398.
- 890 Krasnopolsky, V. A., Gladstone, G. R. 1996. Helium on Mars: EUVE and PHOBOS Data and
implications for Mars' evolution. *J. Geophys. Res.*, 101, 15765-15772.
- 895 Liemohn, M. W., Khazanov, G. V., Moore, T.E., Guiter, S. M. 1997. Self-consistent
superthermal electron effects on plasmaspheric refilling. *J. Geophys. Res.*, 102, 7523-
7536.
- 900 Liemohn, M. W., Frahm, R. A., Winningham, J. D., Ma, Y., Barabash, S., Lundin, R., Kozyra, J.
U., Nagy, A. F., Bougher, S. M., Bell, J., Brain, D., Mitchell, D., Luhmann, J.,
Holmström, M., Andersson, H., Yamauchi, M., Grigoriev, A., McKenna-Lawler, S.,
Sharber, J. R., Scherrer, J. R., Jeffers, S. J., Coates, A. J., Linder, D. R., Kataria, D. O.,
Kallio, E., Koskinen, H., Säles, T., Riihelä, P., Schmidt, W., Roelof, E., Williams, D.,
Livi, S., Curtis, C. C., Hsieh, K. C., Sandel, B. R., Grande, M., Carter, M., Sauvaud, J.-
A., Fedorov, A., Thocaven, J.-J., Orsini, S., Cerulli-Irelli, R., Maggi, M., Wurz, P.,
Bochsler, P., Krupp, N., Woch, J., Franz, M., Asamura, K., Dierker, C. 2006a. Numerical
interpretation of high-altitude photoelectron observations. *Icarus*, 182, 383-395.
- 905 Liemohn, M. W., Ma, Y., Frahm, R. A., Fang, X., Kozyra, J. U., Nagy, A. F., Winningham, J. D.,
Sharber, J. R., Barabash, S., Lundin, R. 2006b. Mars global MHD predictions of
magnetic connectivity between the dayside ionosphere and the magnetospheric flanks.
Space Sci. Rev., 126, 63-76.
- 910 Lundin, R., Zakharov, A., Pellinen, R., Borg, H., Hultqvist, B., Pissarenko, N., Dubinin, E. M.,
Barabash, S. W., Iede, I., Koskinen, H. 1989. First measurements of the ionospheric
plasma escape from Mars. *Nature*, 341, 609-611.
- Lundin, R., Zakharov, A., Pellinen, R., Borg, H., Hultqvist, B., Pissarenko, N., Dubinin, E. M.,
Barabash, S. W., Iede, I., Koskinen, H. 1990. Plasma composition measurements of the

Martian magnetosphere morphology. *Geophys. Res. Lett.*, 17, 877-880.

- 915 Lundin, R., Barabash, S., Andersson, H., Holmström, M., Grigoriev, A., Yamauchi, M., Sauvaud, J.-A., Fedorov, A., Budnik, E., Thocaven, J.-J., Winningham, D., Frahm, R., Scherrer, J., Sharber, J., Asamura, K., Hayakawa, H., Coates, A., Linder, D. R., Curtis, C., Hsieh, K. C., Sandel, B. R., Grande, M., Carter, M., Reading, D. H., Koskinen, H., Kallio, E.,
- 920 Riihela, P., Schmidt, W., Säles, T., Kozyra, J., Krupp, N., Woch, J., Luhmann, J., McKenna-Lawler, S., Cerulli-Irelli, R., Orsini, S., Maggi, M., Mura, A., Milillo, A., Roelof, E., Williams, D., Livi, S., Brandt, P., Wurz, P., Bochsler, P. 2004. Solar wind-induced atmospheric erosion on Mars: First results from ASPERA-3 on Mars Express. *Science*, 305, 1933-1936.
- 925 Lundin, R., Barabash, S., Fedorov, A., Holmström, M., Nilsson, H., Sauvaud, J.-A., 2008a. Solar forcing and planetary ion escape from Mars. *Geophys. Res. Lett.*, 35, L09203, doi:10.1029/2007GL032884.
- 930 Lundin, R., Barabash, S., Holmström, M., Nilsson, H., Yamauchi, Y., Fraenz, M., Dubinin, E. M., 2008b. A comet-like escape of ionospheric plasma from Mars. *Geophys. Res. Lett.*, 35, L18203, doi:10.1029/2008GL034811.
- 935 Mantas, G. P., Hanson, W. B. 1979. Photoelectron fluxes in the Martian ionosphere. *J. Geophys. Res.*, 84, 369-385.
- Padial, N., Csanak, G., McKoy, B. V., Langhoff, P. W., 1981. Photoexcitation and ionization in carbon dioxide: Theoretical studies in the separated-channel static-exchange approximation. *Phys. Rev. A*, 23, 218-235.
- 940 Uluşen, D., and I. R. Linscott, 2008. Low-energy electron current in the Martian tail due to reconnection of draped interplanetary magnetic field and crustal magnetic fields. *J. Geophys. Res.*, 113, E06001, doi:10.1029/2007JE002916.
- 945 Verigin, M. I., Shutte, N. M., Galeev, A. A., Gringauz, K. I., Kotova, G. A., Rfmizov, A. P., Rosenbauer, H., Hemmerich, P., Livi, S., Richter, A. K., Apathy, I., Szegö, K., Riedler, W., Schwingenschuh, K., Steller, M., Yeroshenko, Ye. G. 1991. Ions of planetary origin in the Martian magnetosphere (Phobos 2/TAUS experiment). *Planet. Space Sci.*, 29, 131-137.
- 950 Vignes, D., Mazelle, C. Rème, H., Acuña, M. H., Connerney, J. E. P., Lin, R. P., Mitchell, D. L., Cloutier, P., Crider, D. H., Ness, N. F. 2000. The solar wind interaction with Mars: Locations and shapes of the bow shock and the magnetic pile-up boundary from observations of the MGS/ER experiment on board Mars Global Surveyor. *Geophys. Res. Lett.*, 27, 49-52.
- 955

Table 1.

ELS Voltage to Energy Conversion Factors and Energy Resolution for Each Sector

ELS Sector	Conversion Factor eV/volt	Energy Resolution eV/eV %	ELS Sector	Conversion Factor eV/volt	Energy Resolution eV/eV %
0	7.167	8.653	8	7.275	7.812
1	7.152	8.394	9	7.254	8.094
2	7.141	8.331	10	7.262	8.095
3	7.165	8.579	11	7.255	8.346
4	7.188	8.124	12	7.255	8.297
5	7.625	8.480	13	7.271	7.353
6	7.266	8.194	14	7.253	7.396
7	7.262	7.890	15	7.188	8.843

960

Table 2.

Results of the calculation of number intensity contained in the spectral peaks and supporting information. Case 1 is for the spectrum of Figure 13. Cases 2-23 are selected from the complete data set (5 January 2004 – 25 January 2005).

Sequence Number	Year	Day	Universal Time hh:mm:ss	Number of Spectra Averaged	Spacecraft Potential Volts	Number Intensity $10^6 \text{ elec}/(\text{cm}^2 \text{ s sr})$	Mars Radii X Y Z	ELS Sectors with Photo- electron Peaks
1	2007	170	20:22:59-20:24:09	70	-5.6	5.74 ± 1.26	-3.41 -0.52 -0.88	2
2	2004	114	23:21:59-23:32:00	131	-7.8	3.65 ± 0.72	-2.59 1.55 0.52	3
3	2004	115	07:00:01-07:03:04	40	-8.8	3.71 ± 1.29	-2.53 1.38 0.36	3
4	2004	116	20:47:59-20:58:00	131	-7.9	3.45 ± 0.67	-2.55 1.65 0.76	2
5	2004	120	00:52:01-00:57:00	66	-8.8	4.45 ± 1.12	-2.40 1.48 0.40	4
6	2004	126	01:04:29-01:09:33	66	-7.5	4.36 ± 1.08	-2.15 1.50 0.25	2
7	2004	132	08:08:02-08:16:02	105	-8.8	3.87 ± 0.81	-1.96 1.64 0.50	5
8	2004	307	03:47:58-03:58:04	132	-9.1	4.39 ± 0.77	-1.65 -1.24 -1.58	3
9	2004	314	10:31:02-10:37:02	79	-10.0	3.76 ± 1.05	-1.60 -0.50 -1.69	3
10	2004	358	13:15:01-13:24:02	118	-8.8	4.89 ± 0.74	-2.94 -1.62 0.50	2
11	2004	359	07:04:32-07:08:31	52	-8.7	3.64 ± 1.13	-3.18 -0.30 -2.00	3
12	2004	359	08:39:59-08:45:46	76	-8.8	3.36 ± 0.95	-3.55 -1.35 -0.50	3
13	2004	359	09:12:00-09:17:03	66	-8.8	4.77 ± 1.03	-3.20 -1.55 0.20	3
14	2004	361	15:10:00-15:14:40	61	-8.6	4.07 ± 1.08	-3.00 -1.44 0.37	4
15	2004	362	16:55:00-16:57:59	39	-9.0	3.30 ± 1.39	-3.69 -0.90 -1.00	2
16	2004	364	10:16:01-10:21:00	65	-8.7	4.31 ± 1.10	-3.20 -1.34 0.17	4
17	2004	366	03:07:05-03:11:00	51	-8.6	3.89 ± 1.17	-2.50 -1.35 0.75	3
18	2005	002	20:16:57-20:26:03	119	-7.8	5.07 ± 0.97	-3.60 -0.30 -1.60	3
19	2005	005	03:42:59-03:48:02	66	-7.2	6.01 ± 1.18	-3.15 -1.05 0.15	3
20	2005	007	10:02:32-10:05:31	39	-8.6	3.61 ± 1.43	-2.35 -1.11 0.85	3
21	2005	007	16:42:59-16:50:03	92	-7.8	4.27 ± 0.88	-2.40 -1.10 0.80	4
22	2005	009	09:25:02-09:30:02	65	-8.6	4.86 ± 1.03	-1.69 -1.04 1.10	4
23	2005	009	13:43:25-13:44:31	14	-8.9	3.57 ± 1.72	-3.55 0.02 -1.08	4

965 **Figure Captions**

Figure 1. Simulated ELS Energy Measurement at Mars. The energy measurements below 70 eV are shown both in log space (a) and in linear space (b) with blue points at each energy step, for a simulated ELS measuring Martian electron plasma as described by Mantas and Hanson (1979) (in green). Error bars about each measured value include Poisson statistics. The two-count instrument threshold is shown as a red dotted line.

Figure 2. Shifted Energy Measurements with Respect to the Plasma. The log space (a) and linear space (b) presentations are the same as in Figure 1; however, the measured location has been shifted by half an energy channel width. This simulation shows how measurement appears when plasma peaks are not aligned with energy channel response peaks of the instrument.

Figure 3. The orbit of MEx is shown on 19 June 2007. The MEx trajectory is shown in MSO coordinates as a red curve, ticked at 10 min intervals and labeled every UT hour. Included are highlighted regions where measurements of photoelectron peaks in the ionosphere and tail are generally observed on this spacecraft orbit. The bow shock and magnetopause are drawn for reference using Vignes et al. (2000).

Figure 4. Ion and electron spectrogram from the ionosphere on 19 June 2007. Ions measured by IMA-00 are shown in the top panel with the integral flux of the observed electrons overlaid. Electrons measured by ELS-04 are shown in the bottom panel with the altitude of MEx overlaid. The solar zenith angle (SZA), planetodetic latitude (PdLat), planetodetic longitude (PdLon), solar time (SolTime), and solar latitude (SolLat) of the spacecraft is given along the bottom.

Figure 5. Ionospheric differential energy flux spectrum. Photoelectron energy peaks are shifted by the spacecraft potential, which is about -10.8 volts.

Figure 6. Ion and electron spectrogram from the tail of Mars on 19 June 2007. Format is the same as Figure 4. Distinct and degraded photoelectron peaks are observed.

Figure 7. Differential energy flux spectrum of distinct photoelectron peaks in the Martian tail. Photoelectron energy peaks are shifted by the spacecraft potential, which is about -5.6 volts.

Figure 8. Differential energy flux spectrum of degraded photoelectron peaks in the Martian tail. Photoelectron energy peaks are shifted by the spacecraft potential, which is about -5.6 volts.

Figure 9. Ionospheric electron spectrum. Energy flux is adjusted for the estimated spacecraft potential of -10.8 volts.

Figure 10. Tail electron spectrum showing distinct photoelectron peaks. The energy flux is adjusted for the estimated -5.6 volt spacecraft potential.

Figure 11. Tail electron spectrum with degraded photoelectron peaks. The energy flux is adjusted for the estimated -5.6 volt spacecraft potential.

1010

Figure 12. Statistics on the occurrence of observations of distinct photoelectron peaks. Using ELS-03, A) shows the ratio between the number of samples where distinct photoelectron peaks were observed and the total number of electron spectra sampled by ELS. B) shows the total number of electron spectra sampled by ELS.

1015

Figure 13. Integration details for the distinct photoelectron peaks. Integrations are carried out after computing the differential number flux where points involved in integration are labeled and called out in the text.

1020

Figure 14. Plot of the number intensity values of Table 2. Error bars are based on counting statistics, and instrumental and data processing uncertainties. The dashed line is the average of cases 2-23 of Table 2 and has a value of 4.15×10^6 elec/(cm² s sr). The standard deviation is $\pm 6.70 \times 10^5$ elec/(cm² s sr).

1025 Figure 1. Frahm et al., 2004 Mars electron escape.

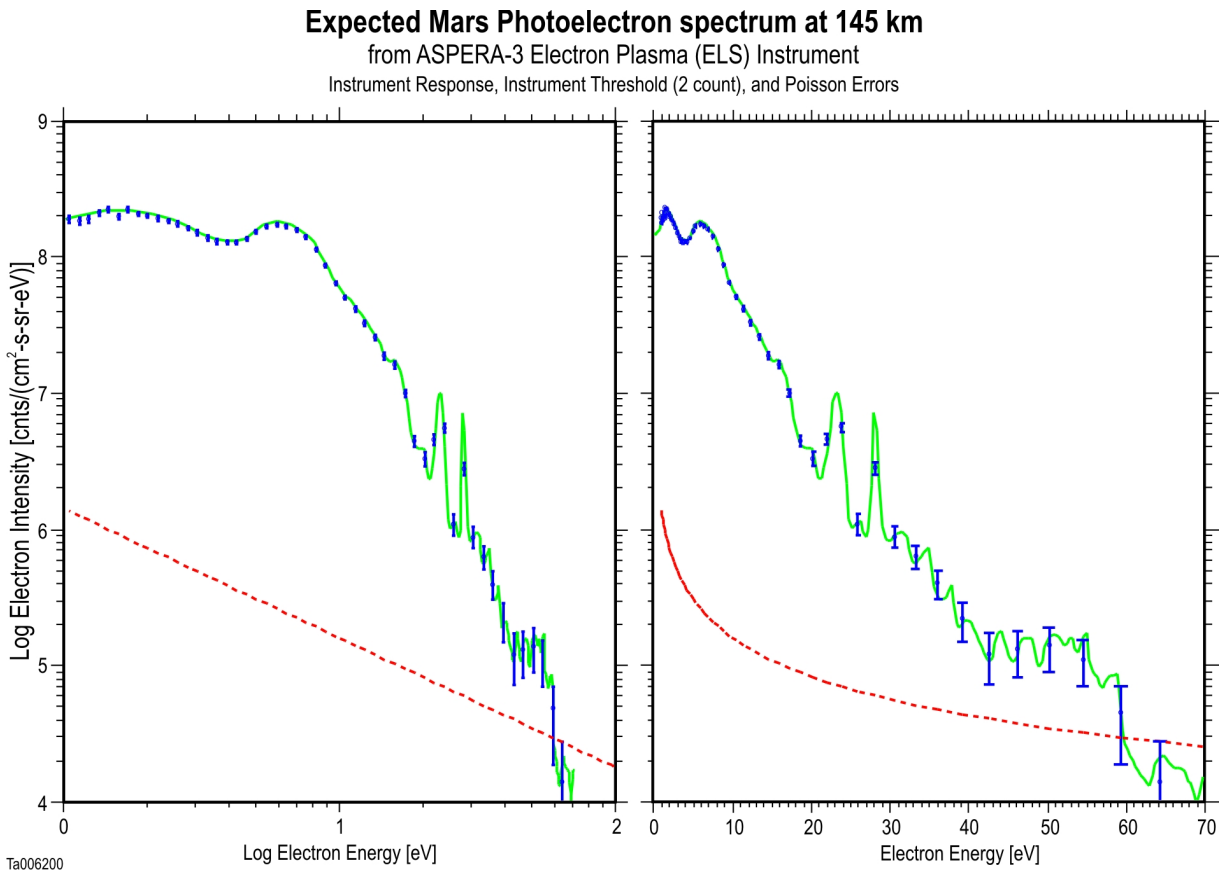


Figure 2. Frahm et al., 2004 Mars electron escape.

1030

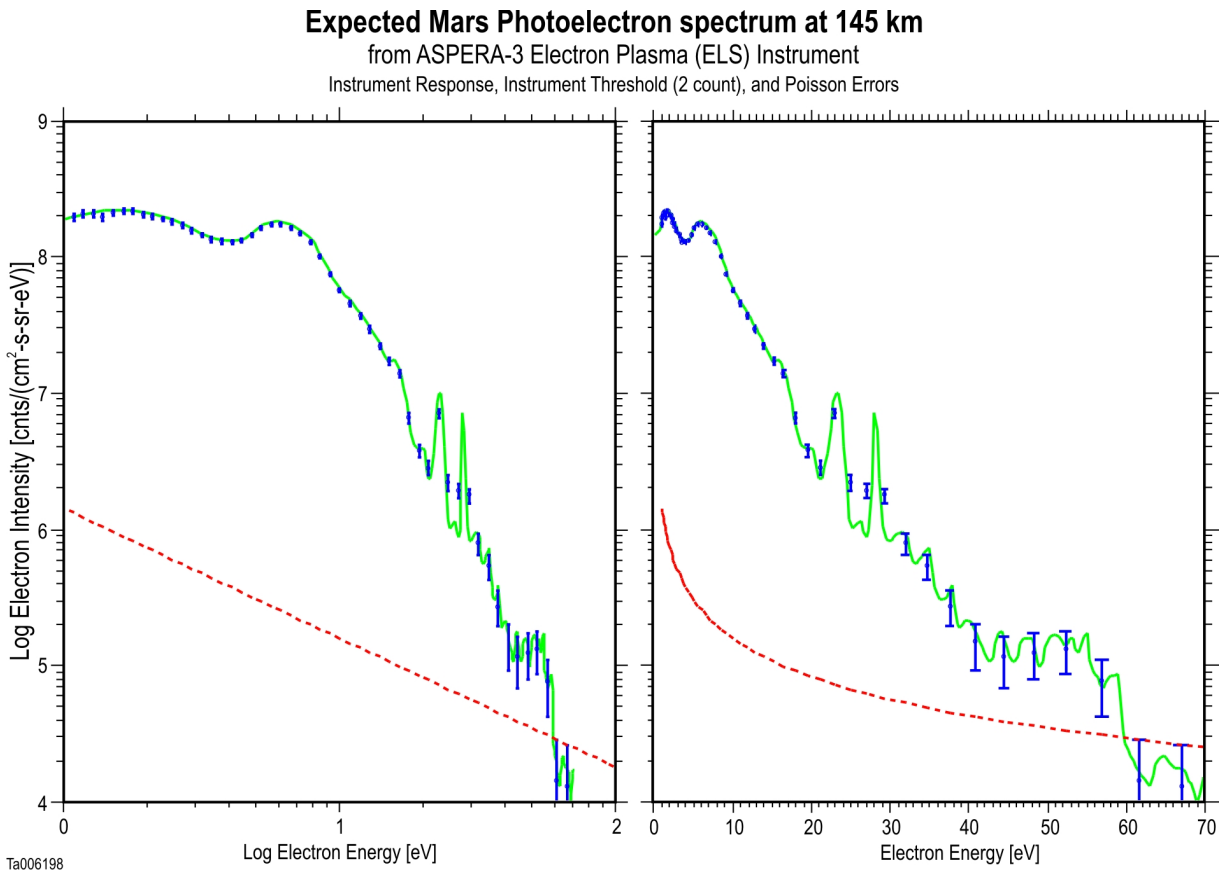


Figure 3. Frahm et al., 2004 Mars electron escape.

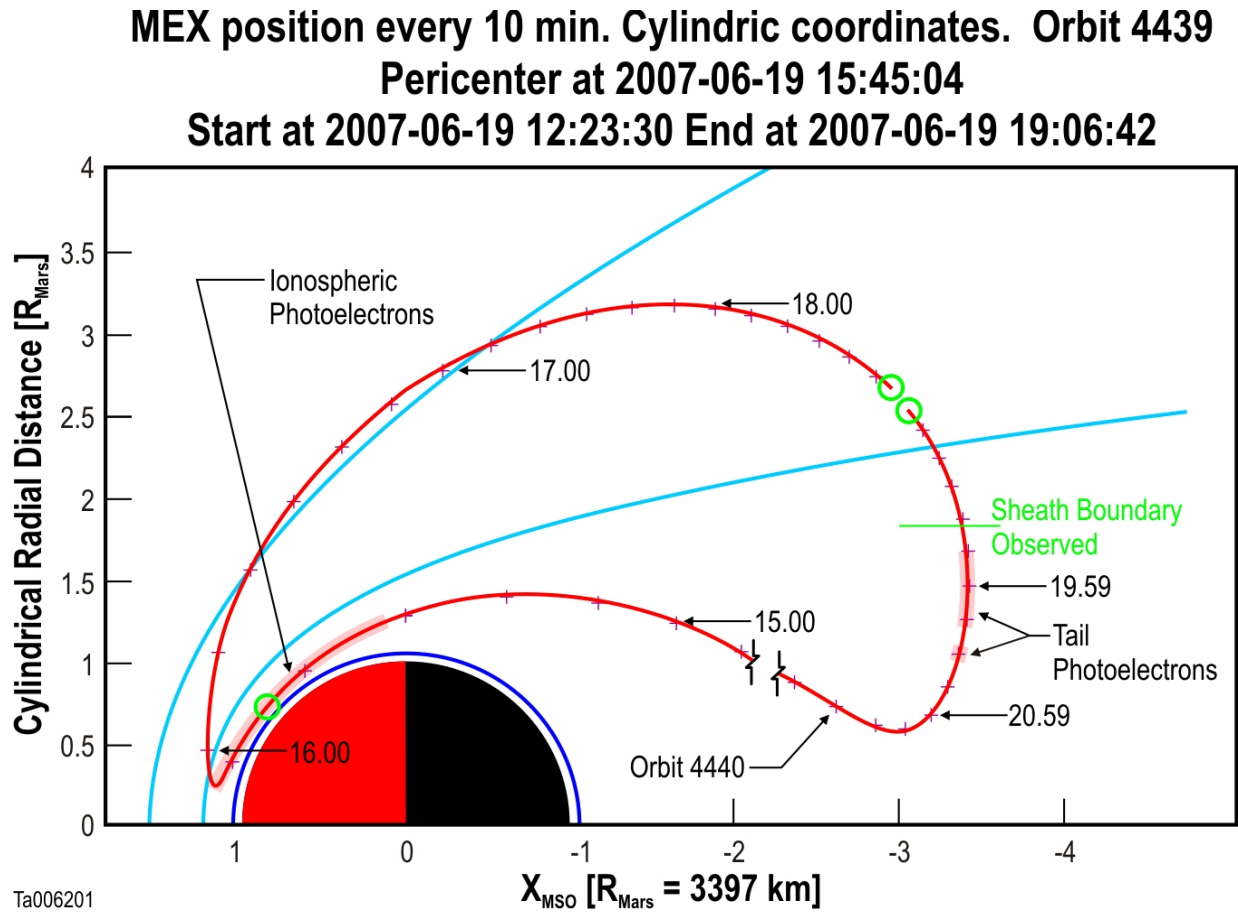
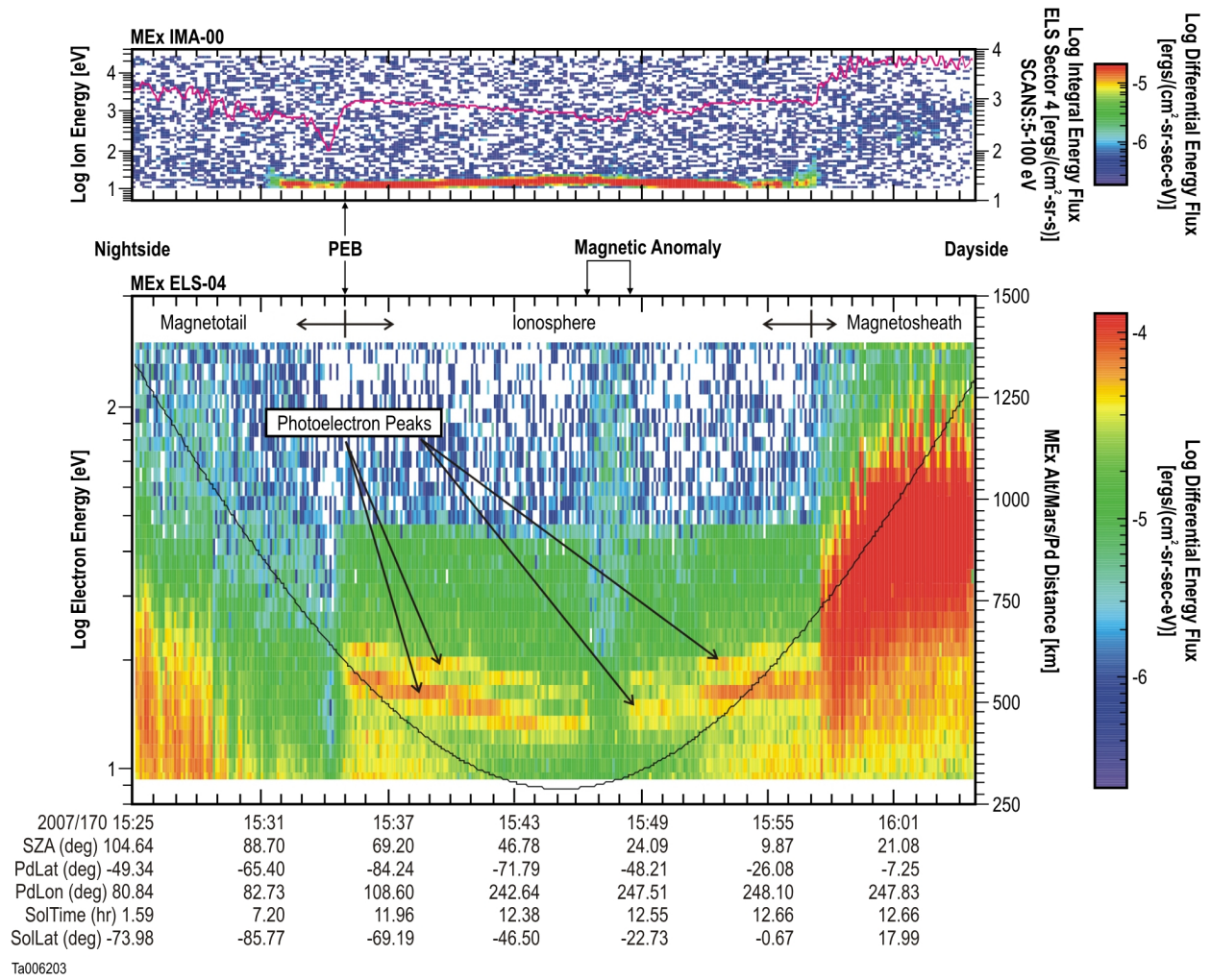
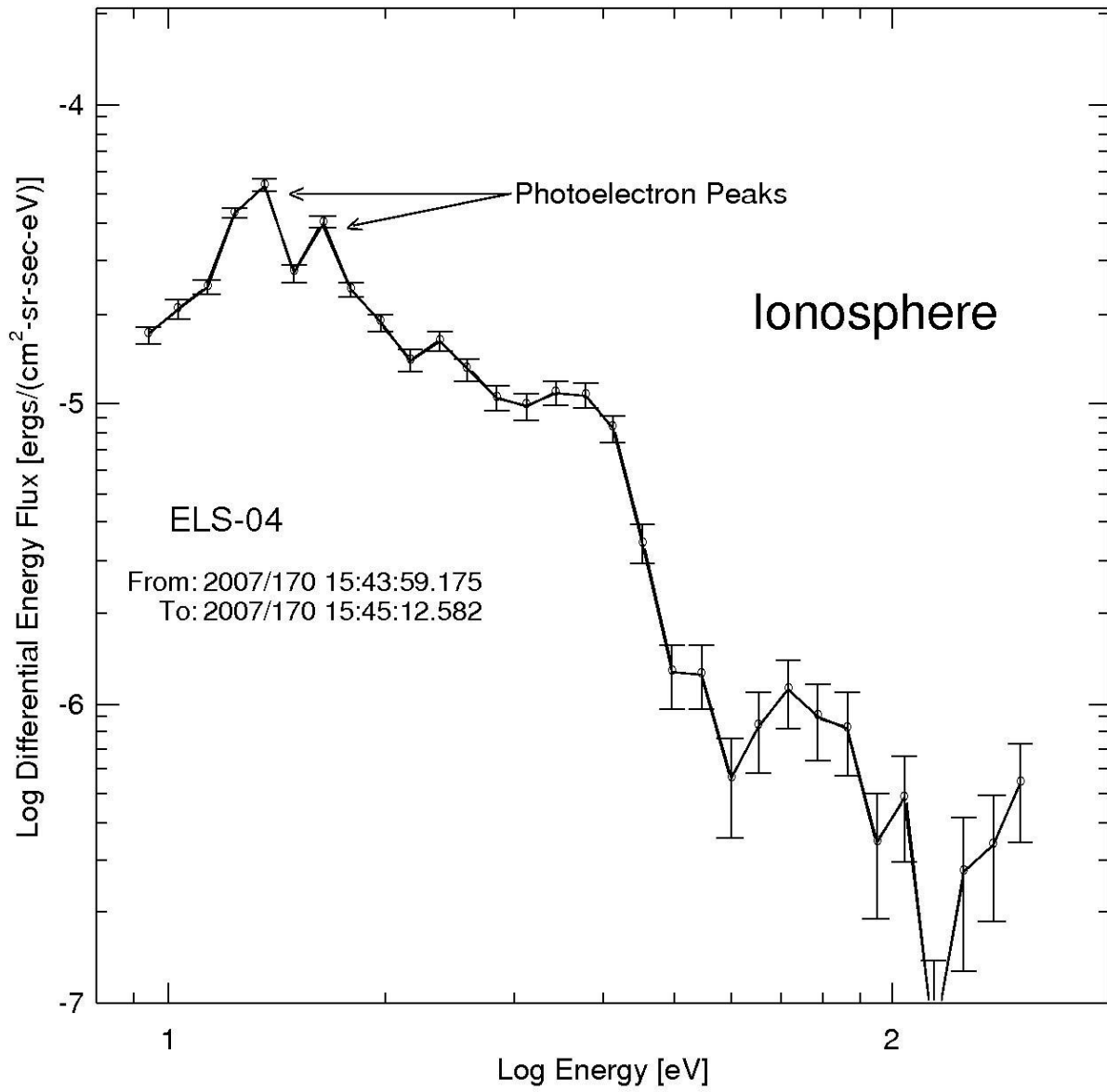


Figure 4. Frahm et al., 2004 Mars electron escape.



1040 Figure 5. Frahm et al., 2004 Mars electron escape.



1045 Figure 6. Frahm et al., 2004 Mars electron escape.

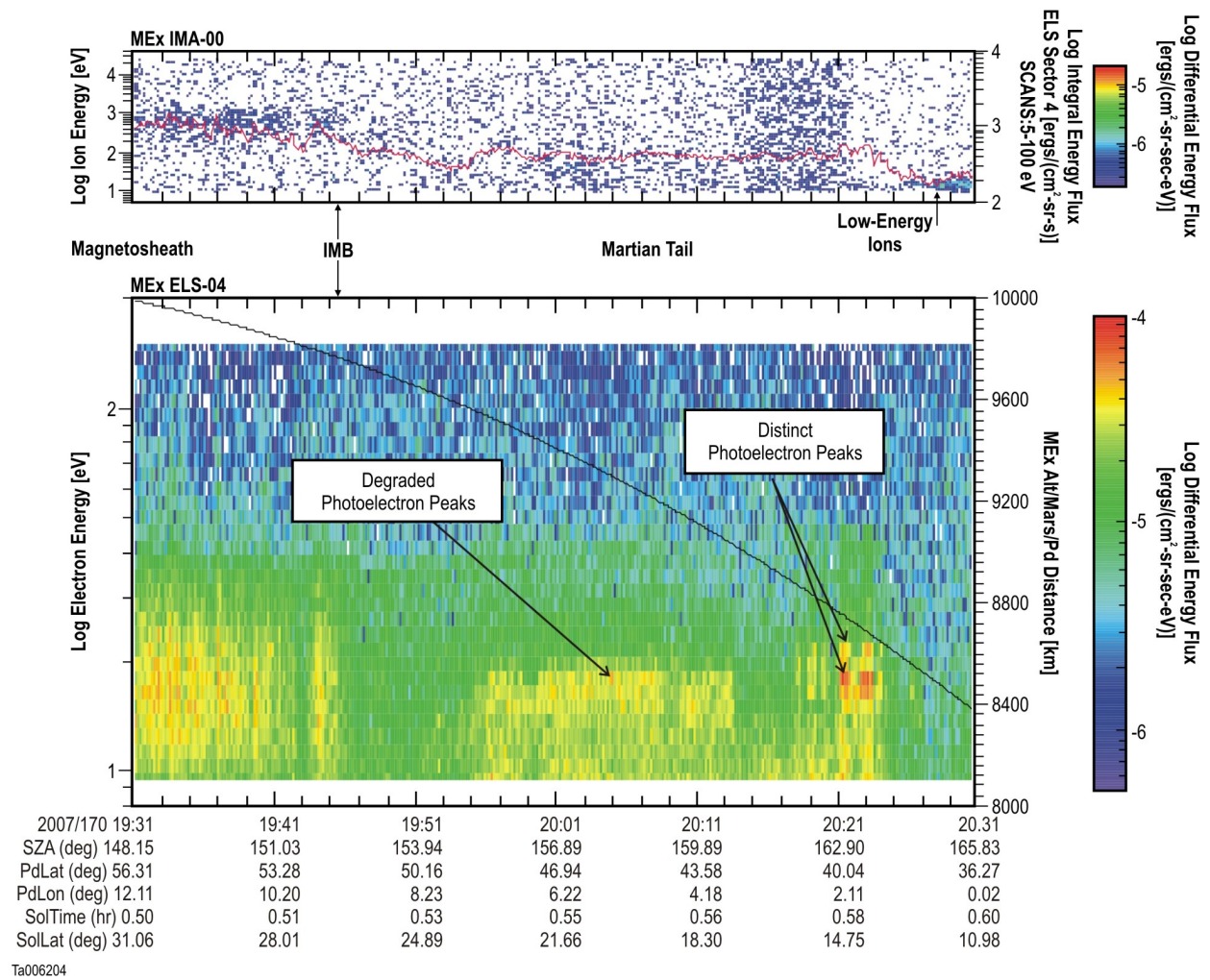


Figure 7. Frahm et al., 2004 Mars electron escape.

1050

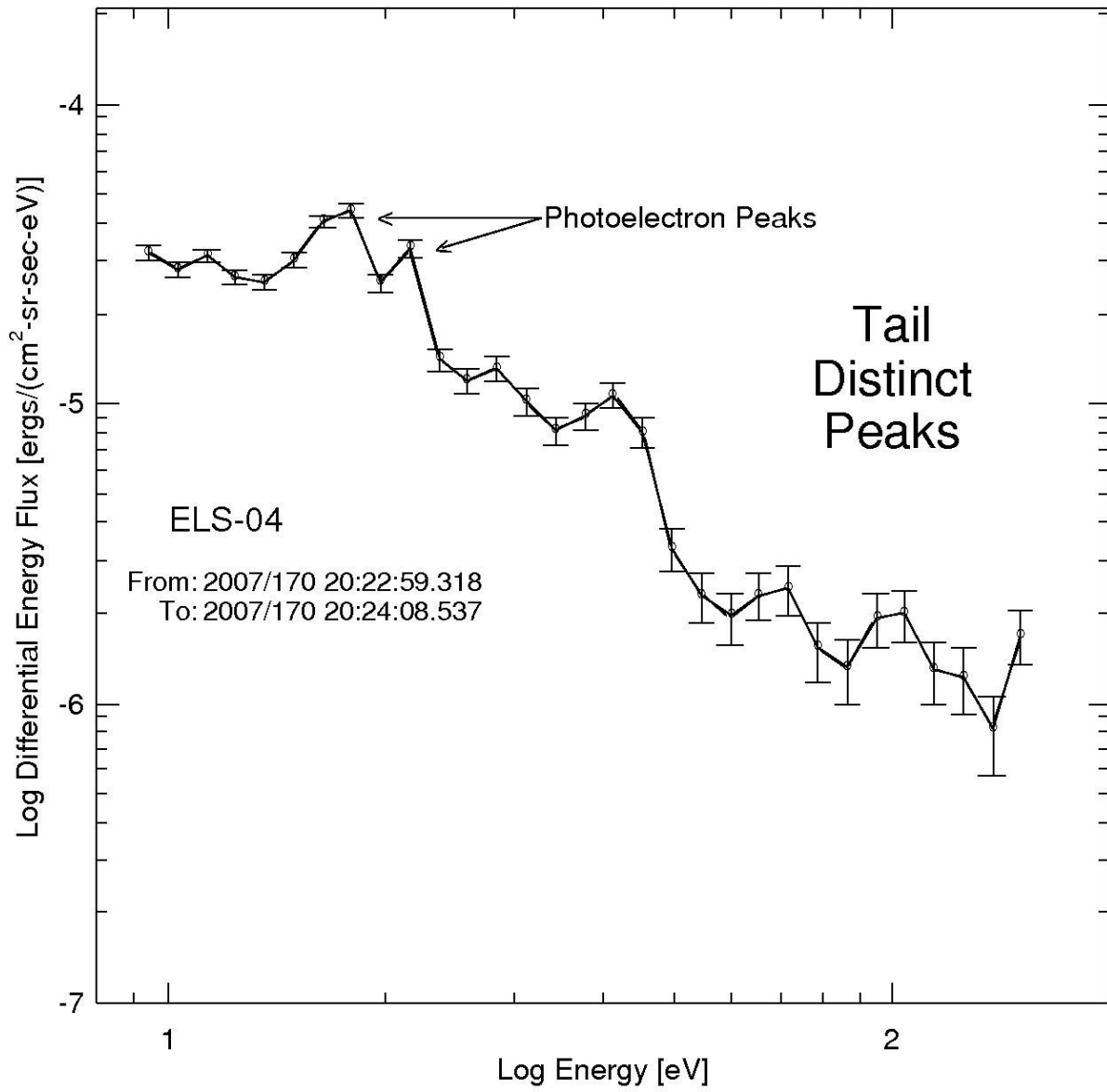


Figure 8. Frahm et al., 2004 Mars electron escape.

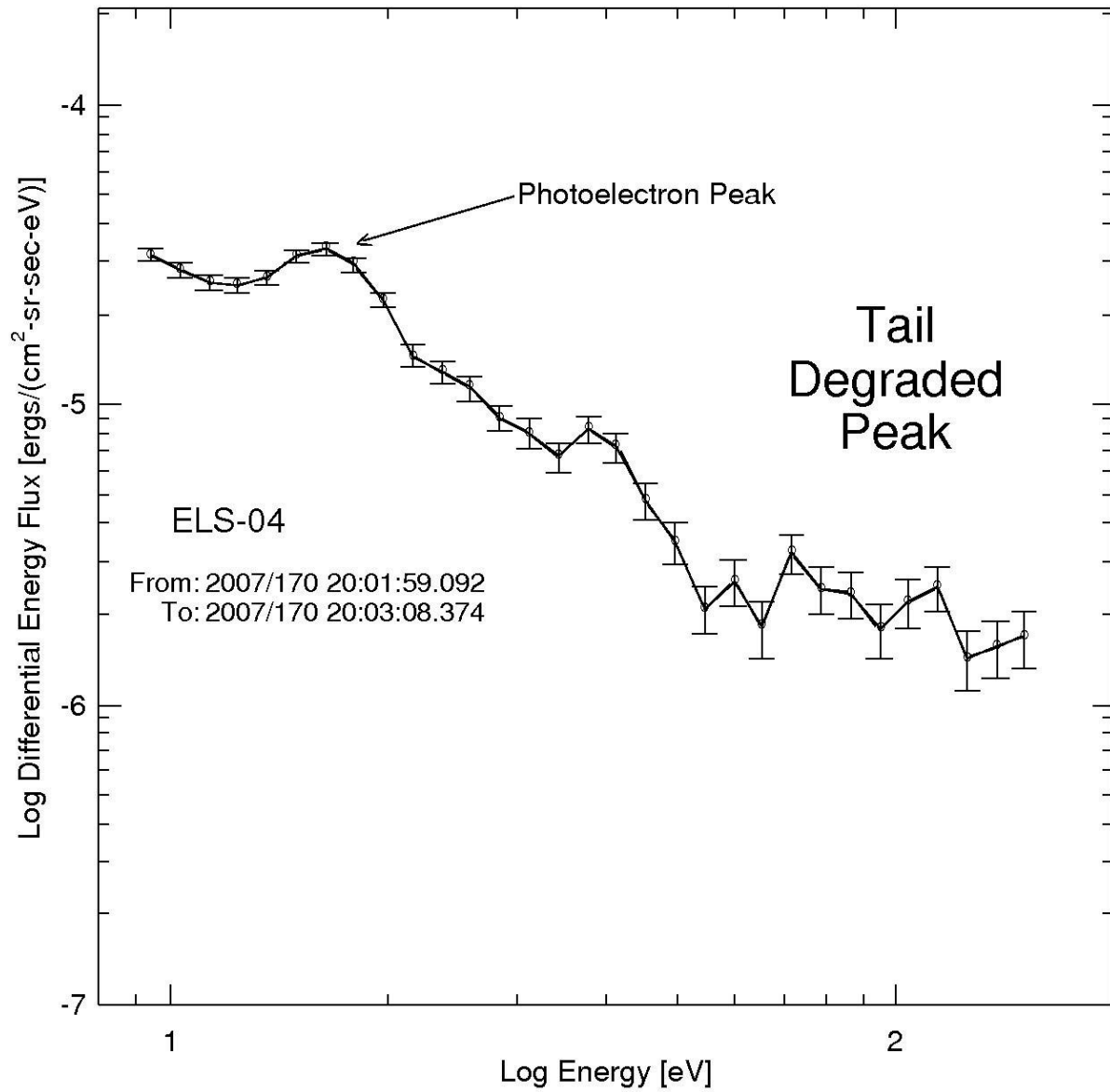
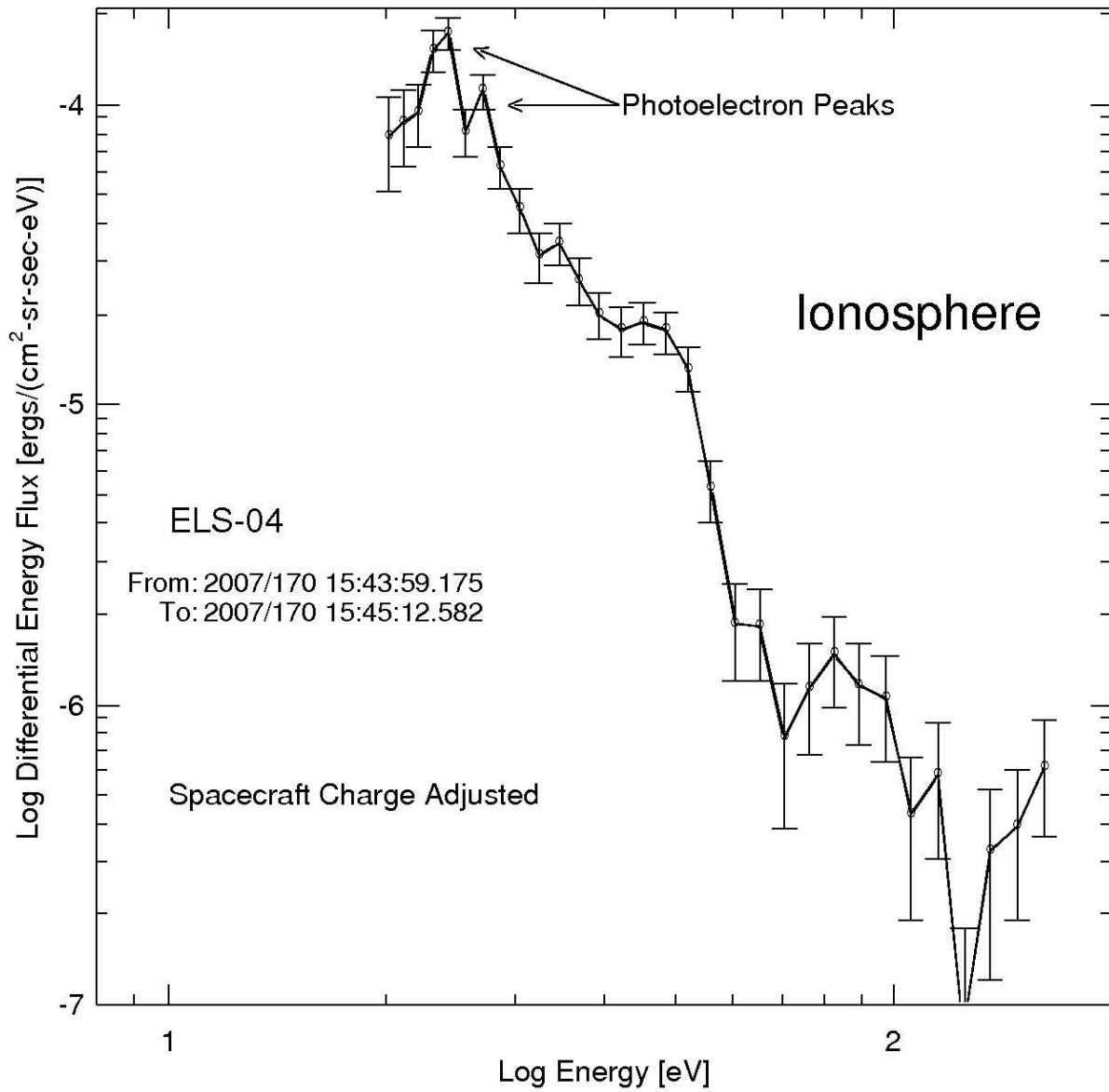


Figure 9. Frahm et al., 2004 Mars electron escape.



1060 Figure 10. Frahm et al., 2004 Mars electron escape.

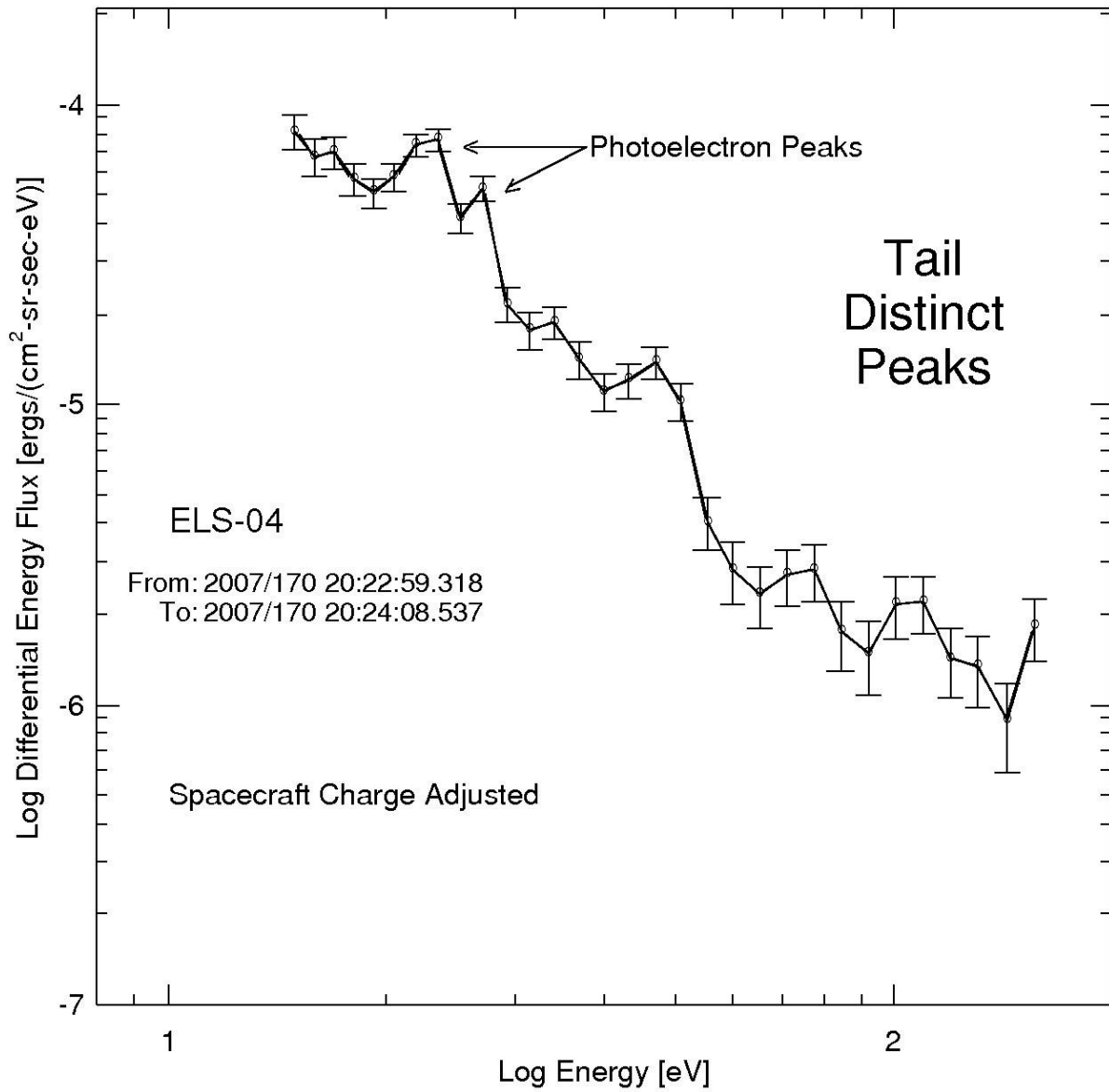


Figure 11. Frahm et al., 2004 Mars electron escape.

1065

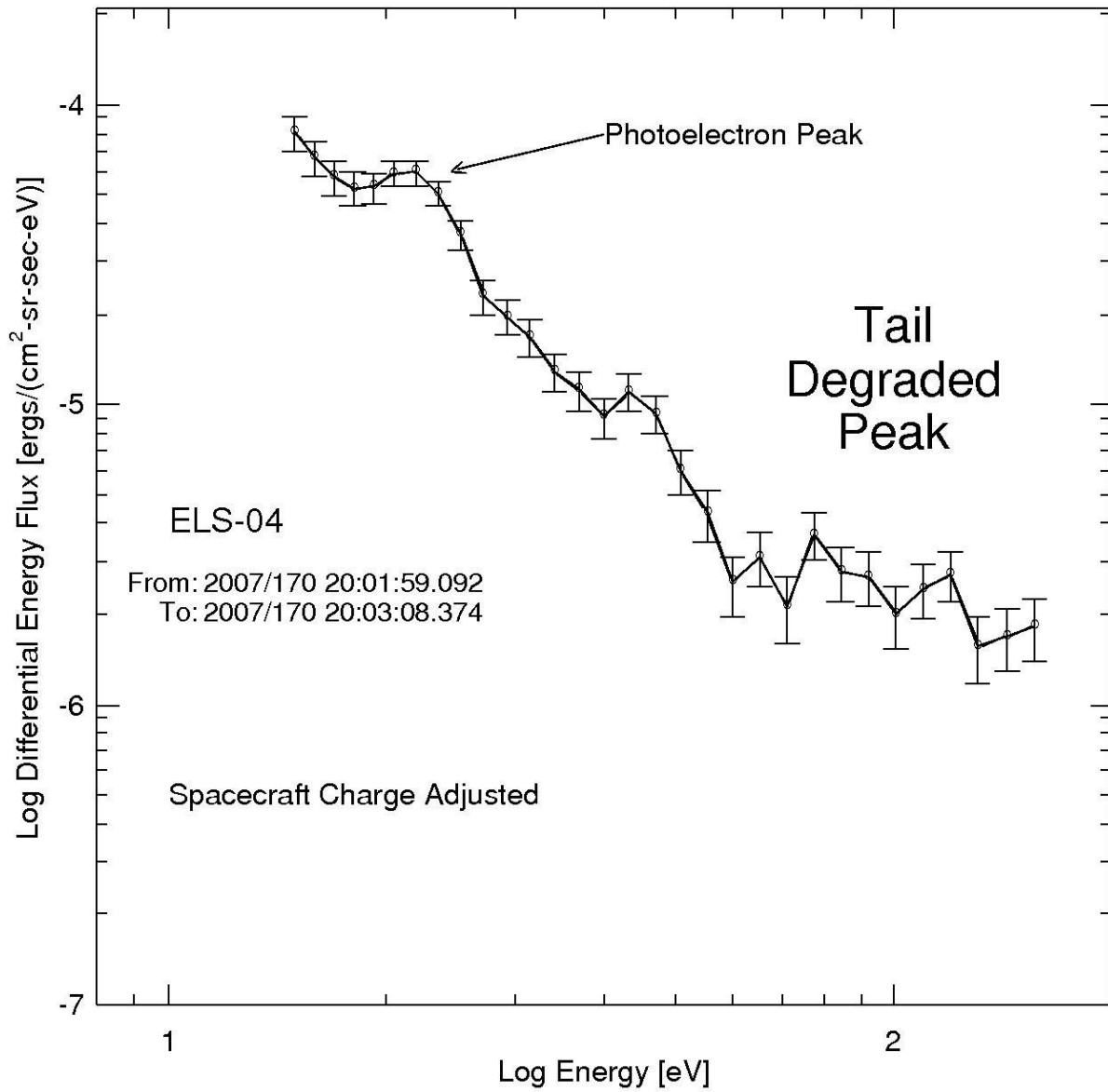
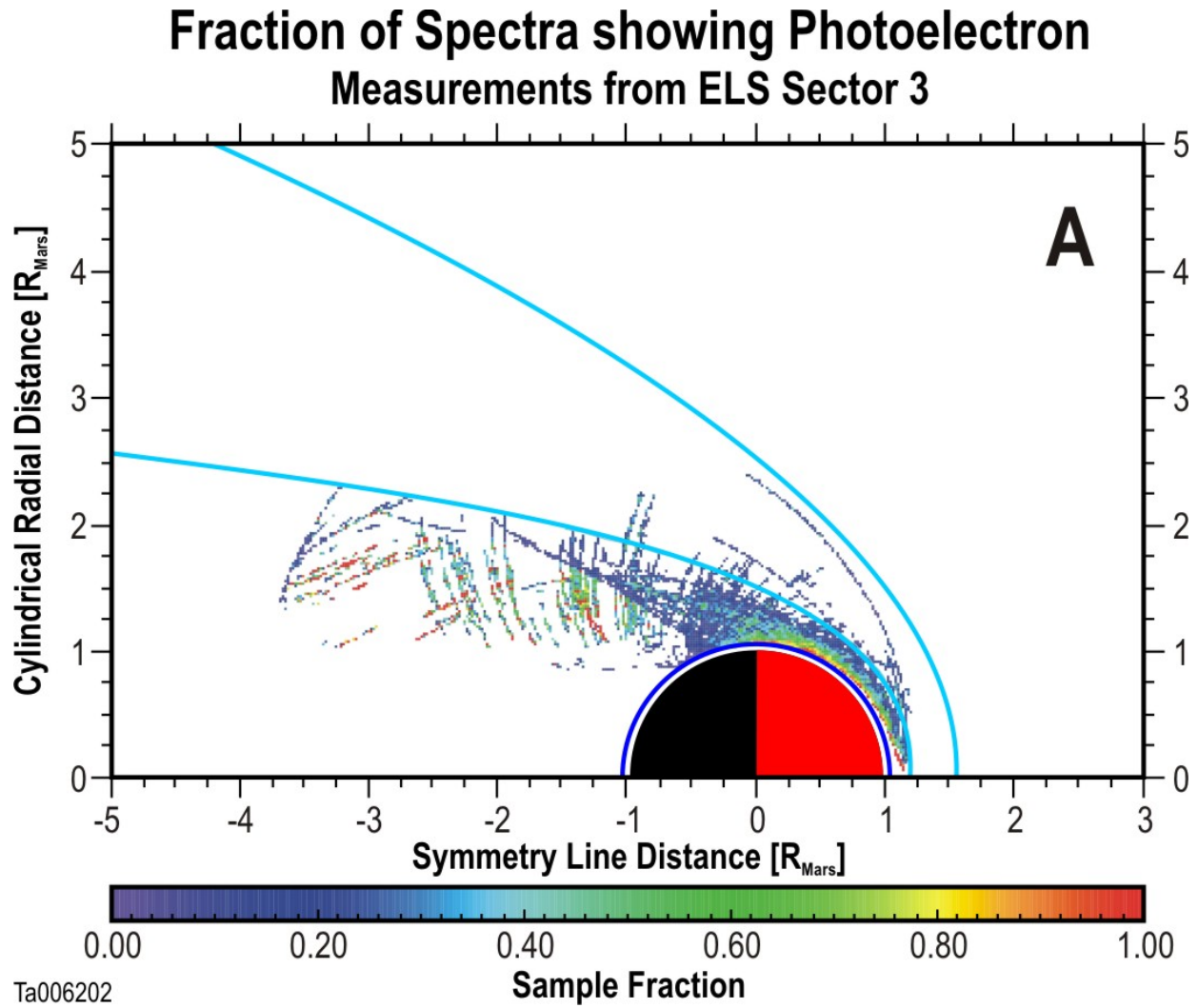


Figure 12a. Frahm et al., 2004 Mars electron escape.

1070



1075 Figure 12b. Frahm et al., 2004 Mars electron escape.

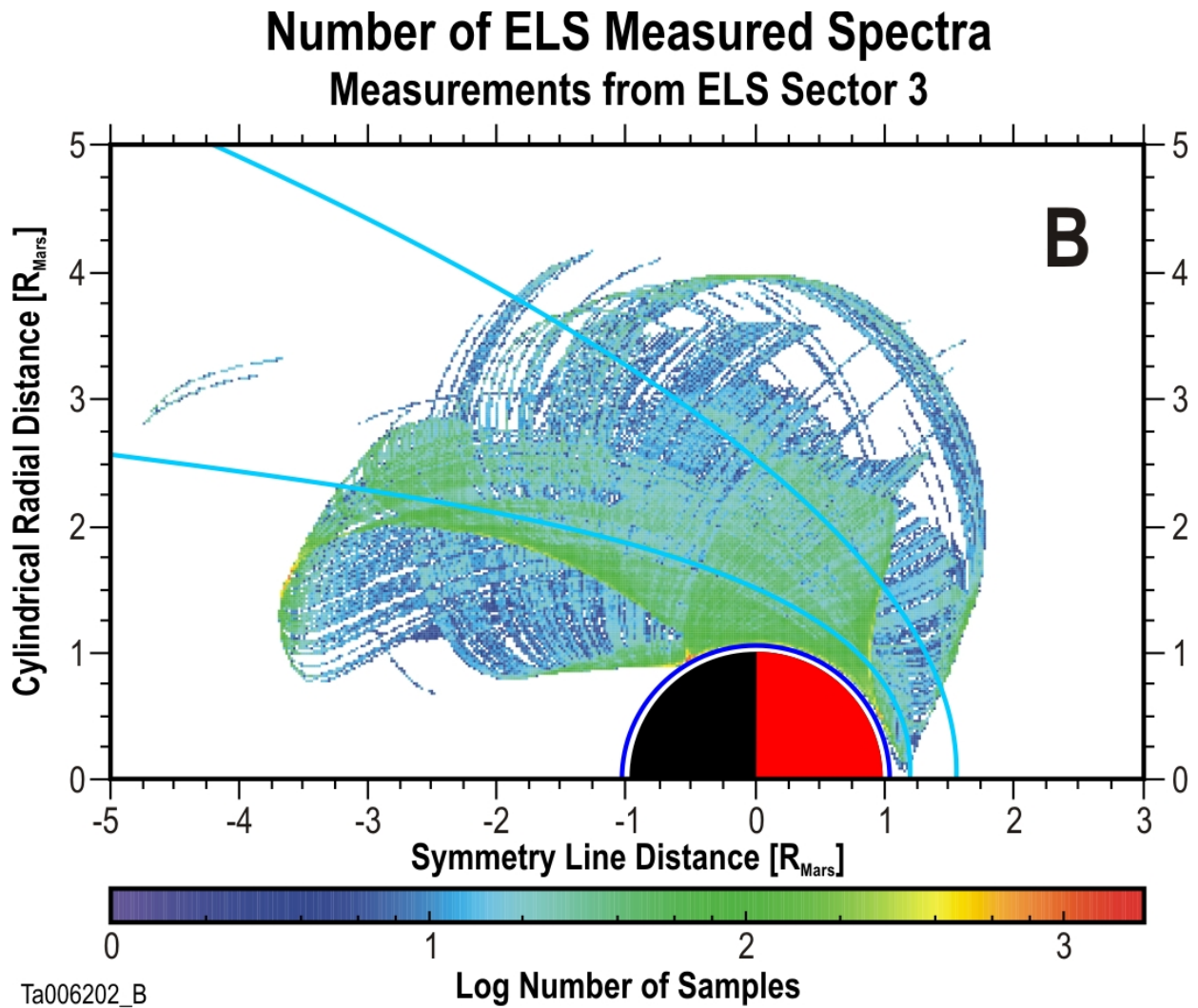
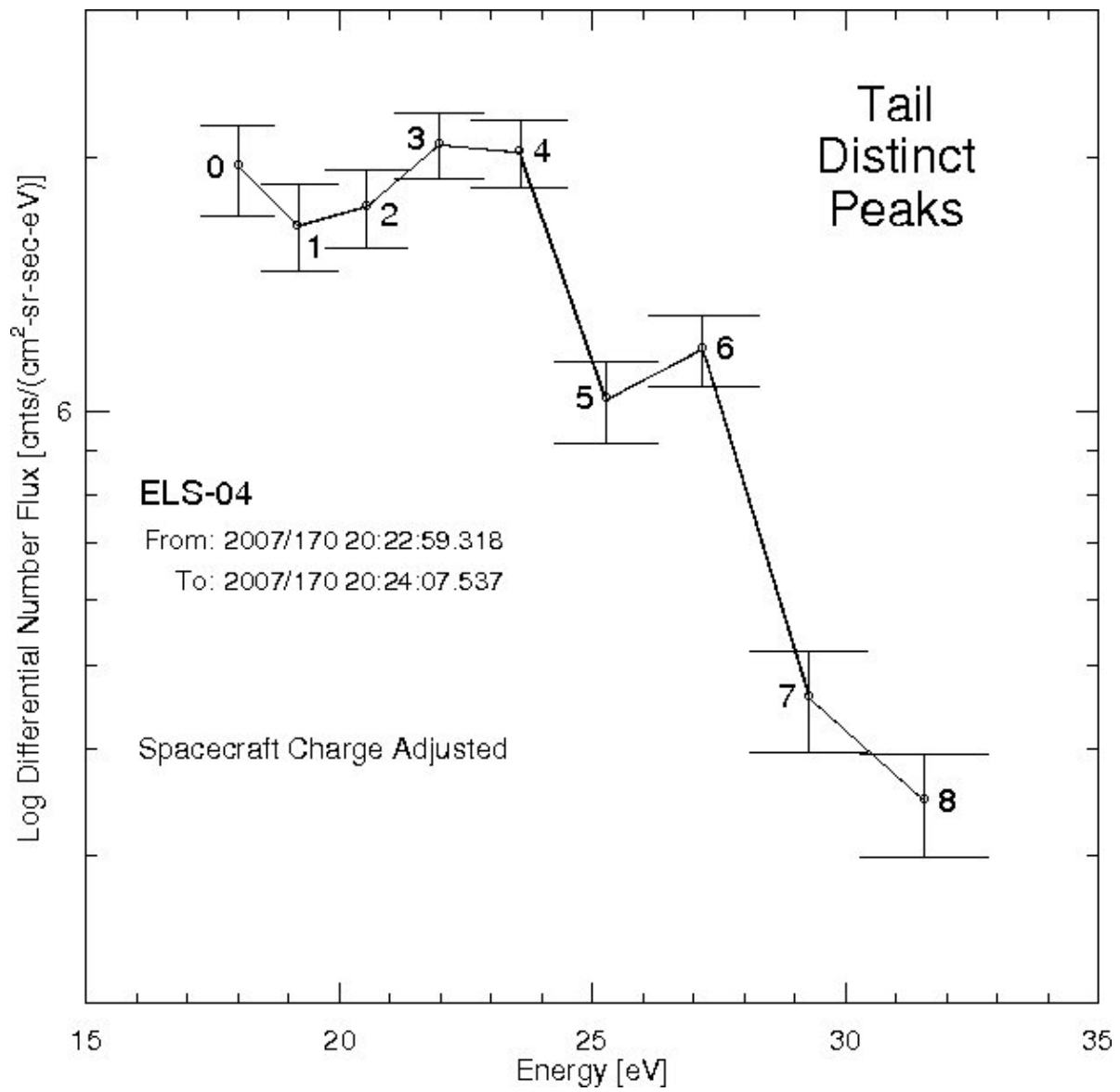


Figure 13. Frahm et al., 2004 Mars electron escape.

1080



1085

1090

Figure 14. Frahm et al., 2004 Mars electron escape.

